

HIGH-PRESSURE LINEAR VISCOELASTICITY MEASUREMENTS

by

Kimberly A. Dennis

A thesis submitted to the Faculty of the University of Delaware in partial fulfillment of the requirements for the degree of Master of Chemical Engineering

Spring 2018

© 2018 Kimberly A. Dennis
All Rights Reserved

HIGH-PRESSURE LINEAR VISCOELASTICITY MEASUREMENTS

by

Kimberly A. Dennis

Approved: _____

Eric M. Furst, Ph.D.

Professor in charge of thesis on behalf of the Advisory Committee

Approved: _____

Eric M. Furst, Ph.D.

Chair of the Department of Chemical and Biomolecular Engineering

Approved: _____

Babatunde A. Ogunnaike, Ph.D.

Dean of the College of Engineering

Approved: _____

Ann L. Ardis, Ph.D.

Senior Vice Provost for Graduate and Professional Education

ACKNOWLEDGMENTS

I would like to thank my family for their love and support throughout this work. My parents have been a constant source of encouragement. My brothers, Chris and Mike, have always had an empathetic ear and wisdom to share. My cat, Colbie, has brought so much joy into my life over the last 2 years. She has always greeted me at the door with the same enthusiasm regardless of the failures or successes.

In addition, I am grateful to Professor Mark A. McHugh (Virginia Commonwealth University) and his lab members, Dr. Babatunde (BB) Bamgbade, Dr. Rajendar (Reddy) Mallepally, and Aaron J. Rowane for their guidance with high-pressure cell assembly and troubleshooting. I would also like to thank Professor Norman J. Wagner for use of the AR-G2 rheometer, high-shear mixer, and moisture analyzer as well as lab members, Dr. Kevin J. Whitcomb and Julie Hipp, for helpful rheology discussions. Thanks also to Professor Christopher J. Roberts and lab member Cesar Calero-Rubio for use of the refractometer and densiometer. In addition, thanks to Professor Christopher J. Kloxin for fruitful discussions about high-pressure diffusing wave spectroscopy. I am also very appreciative of Dr. Weihua Deng for help with lab equipment and Alfred (Al) Lance for machining the high-pressure cell.

This work was supported by Schlumberger.

TABLE OF CONTENTS

LIST OF TABLES	vi
LIST OF FIGURES	vii
ABSTRACT	xii
 Chapter	
1 INTRODUCTION AND BACKGROUND	1
1.1 Motivation and Goals	1
1.2 Hydraulic Fracturing	2
1.3 Microrheology	5
1.4 Multiple Particle Tracking	6
1.5 Diffusing Wave Spectroscopy	6
REFERENCES	19
2 MATERIALS AND METHODS	23
2.1 Materials	23
2.2 Multiple Particle Tracking	24
2.3 Diffusing Wave Spectroscopy	25
2.4 Density Measurements	25
2.5 Refractometry	25
2.6 Mechanical Rheology	25
2.7 High-pressure Diffusing Wave Spectroscopy	26
2.7.1 High-pressure Cell and System Design	26
2.7.2 Key Considerations	32
2.7.3 Operating Regime	37
2.8 Purely Viscous Samples Data Analysis	38
2.9 Data Analysis of a Viscoelastic Fluid	42
REFERENCES	44

3	VISCOSITY OF 1-PROPANOL-WATER MIXTURES	47
3.1	High-pressure Water Viscosity	47
3.2	High-pressure Aqueous 1-Propanol Viscosity	51
	REFERENCES	56
4	CONCLUSIONS AND FUTURE WORK	57
4.1	Conclusions	57
4.2	Physically Crosslinked Guar Gum Under Pressure	57
4.3	Experiment Modification	66
4.4	Borate Crosslinked Poly(vinyl) Alcohol	67
	REFERENCES	68
Appendix		
	LASER MAINTENANCE	70
	REFERENCES	77

LIST OF TABLES

2.1	Volume change with increase in pressure	28
2.2	Gravitational Péclet Pe_g for water and 1-propanol with $1 \mu\text{m}$ polystyrene spheres.	38

LIST OF FIGURES

1.1	Simplified schematic of fracturing showing a vertical well expanded into a horizontal well. From the horizontal well, fractures in the subterranean hydrocarbon rich shale are visible.	3
1.2	Pressure dependent viscosity of 0.3 wt% guar solution crosslinked with 60 ppm boron at 30°C and pH 9. Data taken from Parris et al. 2008 [17].	4
1.3	Schematic of photon propagation in point source illumination in the transmission geometry.	8
1.4	Scattering (l) and photon (l^*) mean free paths as a function of particle size (a) scaled by scattering wave vector (k) for hypothetical 1 vol% particle dispersion.	10
1.5	Schematic of point source illumination in the transmission geometry with gradient refractive index (GRIN) lens.	12
1.6	Schematic of plane wave illumination in the backscattering geometry.	13
1.7	Theoretical $g_2(\tau) - 1$ as a function of delay time for point source, plane wave, and gaussian beam with $l^* = 220, 290,$ and $450 \mu\text{m}$. The hypothetical samples correspond to 1 vol% aqueous dispersions of 0.6, 1.1, and $2.2 \mu\text{m}$ diameter polystyrene microspheres in a 4.5 mm cuvette at 20 °C.	16
1.8	Theoretical $g_2(\tau) - 1$ and $g_1(\tau)$ as a function of delay time for point source and plane wave with $l^* = 220 \mu\text{m}$. The hypothetical sample corresponds to a 1 vol% aqueous dispersion of $1.1 \mu\text{m}$ diameter polystyrene microspheres in a 4.5 mm cuvette at 20 °C.	17
1.9	Theoretical $g_2(\tau) - 1$ as a function of delay time for point source and plane wave with $l^* = 290 \mu\text{m}$ for $1.1 \mu\text{m}$ diameter polystyrene dispersion in water for 1, 4.5, and 10 mm pathlengths at 20 °C.	18

2.1	High-pressure cell schematic with cell body length and inner and outer diameters.	28
2.2	Schematic of high-pressure system setup.	28
2.3	Image of the high-pressure system and cell integrated into a light scattering setup.	29
2.4	Image of cylindrical sapphire window used to permit light scattering through the cell at elevated pressures.	29
2.5	Assembled high-pressure cell resting in aluminum jaws. Side left connection goes to sample gauge and piston. Top port is shown with plug.	29
2.6	Piston with (right) and without deformation (left) caused by bottoming out.	31
2.7	Image of one fabricated polyimide o-ring with inner and outer diameter dimensions.	31
2.8	High-pressure cell pressure validation. The system was initially pressurized to 210 MPa and relaxed over time to 197 MPa.	31
2.9	Experimental setup to assess effect of birefringence. In the laser beam path, a 4.5 mm cuvette is shown between 2 sapphire windows.	33
2.10	Normalized $g_2(\tau) - 1$ for 5 window setups with 0.5 vol% polystyrene in water in a 4.5 mm cuvette.	34
2.11	The hypothetical $g_2(\tau) - 1$ for 1 μm polystyrene particle dispersion with an 11.8 mm pathlength at atmospheric (0.1 MPa, 260 μm) and elevated pressures (206 MPa, 280 μm).	36
2.12	Transmission DWS operating regime for 0.5 vol% 1 μm polystyrene beads in 11.8 mm pathlength at 25°C.	37
2.13	Experimental $g_2(\tau) - 1$ for 1.05 vol% polystyrene spheres in a 4.5 mm cuvette in plane wave and point source transmission mode.	40
2.14	Experimental $g_2(\tau) - 1$ and $g_1(\tau)$ for 1.05 vol% polystyrene spheres in a 4.5 mm cuvette in plane wave and point source transmission mode.	40

2.15	Experimental $g_2(\tau) - 1$ for 1.05 vol% polystyrene spheres in a 4.5 mm cuvette in point source transmission with fit.	41
2.16	Experimental $g_2(\tau) - 1$ for 1.05 vol% polystyrene spheres in a 4.5 mm cuvette in plane wave transmission with fit.	41
2.17	Normalized $g_2(\tau) - 1$ for 1, 6.7, and 12.2 wt% 200 kDa PEO with 1 wt% 1 μm polystyrene spheres at 21°C in the HPC. The intermediate decay region was fit as denoted by the dotted line. Water is shown for reference.	43
2.18	The mean square displacement (MSD) scaled by probe radius for 6.7, and 12.2 wt% 200 kDa PEO compared to literature data[12]. Water and logarithmic slope of 1 are shown for reference.	43
3.1	Normalized $g_2(\tau) - 1$ for 0.5 vol% polystyrene beads in water in the high-pressure cell.	49
3.2	Normalized $g_2(\tau) - 1$ for 0.5 vol% polystyrene beads in water in the high-pressure cell with fit.	49
3.3	High-pressure water viscosity at 21°C.	50
3.4	Chemical structure of 1-propanol.	52
3.5	An image of fluorescent micrometer-diameter polystyrene spheres in 1-propanol that shows the probes are colloidally stable.	52
3.6	Experimental $g_2(\tau) - 1$ for 0.5 vol% polystyrene beads in 1-propanol with a mole fraction of 0.84 as a function of pressure. Open circle and triangles show repeat experiment after pressure ramp. Water is shown for reference.	54
3.7	Experimental $g_2(\tau) - 1$ for 0.5 vol% polystyrene beads in 1-propanol with a mole fraction of 0.84 as a function of pressure with fit. Water shown for reference.	54
3.8	Experimental data (filled) with 90% confidence intervals (smaller than points) at 21°C and literature data at 10 and 25 °C [6] showing pressure dependence of aqueous 1-propanol solutions. Data for 21 °C were linearly interpolated.	55
4.1	Guar gum with vicinal hydrogens highlighted in red.	58

4.2	Adapted figure of physical crosslinking of vicinal hydroxyls by borate from a 1:1 complex (top) to a 2:1 complex (bottom) [3].	58
4.3	Modified loading limit for high-pressure diffusing wave spectroscopy instrument.	60
4.4	Elastic modulus for 0.3 wt% purified guar gum with 60 ppm boron determined from mechanical rheometry using a 60 mm, 2° cone. . .	60
4.5	Image of 0.3 wt% guar gum with 60 ppm boron. Geometry shown is a 40 mm 4° cone and peltier plate.	61
4.6	Image of 0.3 wt% guar gum with 40 ppm boron. Geometry shown is a 40 mm 4° cone and peltier plate.	61
4.7	Visual operating regime for precipitate (P), solution (S), and gel (G). Observations taken at 30-60 minutes and again overnight.	62
4.8	Normalized $g_2(\tau) - 1$ for purified guar gum with 0.5 vol% polystyrene spheres. Water is shown for reference.	64
4.9	Normalized $g_2(\tau) - 1$ for crosslinked guar gum with 20 ppm boron and 0.5 vol% polystyrene spheres. Water is shown for reference.	64
4.10	Creep compliance for intermediate delay times.	65
4.11	Poly(vinyl) alcohol structure.	67
A.1	Image of new pump valve used to restrict or allow access to the cooling water from a heat exchanger.	71
A.2	Image of laser output suggestive of transverse modes.	72
A.3	Schematic of laser cavity. The dotted line indicates the path of the laser beam resonance. All of the laser light is not reflected by the output mirror to allow for lasing.	73
A.4	Image of front Brewster window facing upwards. This window is cleaned from top to bottom.	73
A.5	Image of rear Brewster window facing downwards. This window is cleaned from bottom to top.	73

A.6	Front Brewster window face before cleaning by the “Hemostat and Lens Tissue Method”.	74
A.7	Front Brewster window face after cleaning by the “Hemostat and Lens Tissue Method”.	74
A.8	Normalized $g_2(\tau) - 1$ of samples before and after laser alignment. The sample is 1 vol% 1.04 μm polystyrene probes in water in 1 and 4.5 mm cuvettes.	76

ABSTRACT

Complex fluids from biological systems to polymeric solutions and gels experience elevated pressures due to environmental and processing conditions, which may impact the fluid performance. Tunable pressure-dependent fluid behavior is desirable for oilfield applications to optimize hydrocarbon recovery. Oilfield fluids are used to help transport and suspend solids, reduce friction pressure, and prevent fluid loss. Key to these fluid performance metrics is the fluid rheology. Depending upon the composition and flow conditions, the fluid can behave as a purely viscous or viscoelastic fluid. By selecting the composition, the flow properties can be optimized for specific functions, such as, suspending proppants to keep fractures open or retaining fluid downhole.

High-pressure measurements may be performed using falling body, pressure-driven, and rotational devices. Falling body rheometers use a stationary object in a moving fluid or a stationary fluid with a mobile object to obtain viscosity measurements. Pressure-driven devices force a fluid through a capillary and obtain pressure drop and volumetric flow rate to obtain the viscosity. These techniques are restricted in the material properties that may be obtained and their application to non-Newtonian fluids. Rotational rheometers apply a shear or oscillatory stress or strain to the fluid to obtain viscoelastic properties, however, this technique is often pressure-limited. Overall, high-pressure viscoelastic measurements can be challenging for mechanical rheometers.

To address these shortcomings, a passive microrheology experiment has been designed and validated to measure the linear viscoelasticity of complex fluids at high pressures. The apparatus incorporates a steel alloy sample chamber with dual sapphire windows into a simple diffusing-wave spectroscopy (light-scattering) device and

is capable of both transmission and backscattering geometries. The measured light intensity correlation from the Brownian motion of polystyrene probe particles dispersed in the sample is interpreted using the Generalized Stokes-Einstein Relation to determine the material linear viscoelasticity. This high-pressure microrheology instrument is validated by measuring the viscosity change of water and 1-propanol over pressures from 0 to 172.4 MPag at ambient temperature.

Complimentary mechanical and microrheology measurements are performed at ambient pressure on stimulation fluids containing a crosslinked guar gum biopolymer before the measurement is performed at elevated pressures. We investigate the effect of crosslinker density on rheological properties at frequencies up to 1 MHz and pressures of 200 MPag, expanding the accessible range of experimental conditions beyond those of existing rheological measurement techniques.

Chapter 1

INTRODUCTION AND BACKGROUND

1.1 Motivation and Goals

Complex fluids often experience a range of pressures from environmental and processing conditions, which may impact flow properties and the desired performance. Approximately 11 km below the ocean surface, in the Challenger Deep, live piezophiles which have optimum growth rates at ~ 76 MPa [1, 2]. In contrast, certain dairy emulsions are processed at pressures up to 1,000 MPa to deactivate microorganisms [3]. At intermediate pressures of 70-275 MPa, polymer solutions and gels are processed for hydraulic fracturing [4]. Pressure affects material properties such as rheology, so it is essential to understand pressure effects to predict processability.

Despite the concomitant nature of temperature and pressure, temperature effects have been studied more than pressure effects due to the limitations of mechanical rheometry equipment [5]. High-pressure macrorheology performed using pressure-driven, falling-body, and rotational devices may be inaccurate or limited by material composition and shear rate under pressure [6]. Common mechanical rheometers are also limited to a frequency range of 10^{-7} - 10^2 Hz [7] due to torque limits and inertial effects. While mechanical rheometers are extensively used for fluid rheological characterization, they can be difficult to use and inaccurate under extreme conditions, such as high pressure. To address these shortcomings, a high-pressure passive microrheology experiment is designed and validated to measure the linear viscoelasticity of complex fluids.

The objectives of this research are to integrate a high-pressure cell into a light scattering apparatus, validate the high-pressure setup with model systems, and extend the measurement to viscoelastic soft materials. The high-pressure cell [8] was

redesigned for the current light scattering system and was validated using model systems and thoroughly designed operating procedures and parameters. Preliminary experimental work was also performed on guar gum as it is extensively used in aqueous mixtures of polymer and sand, referred to as stimulation fluids, for hydraulic fracturing of shale oil and gas [9, 10]. A thorough understanding of the viscoelastic behavior is necessary to design these fluids to suspend proppants, which keep the fractures from collapsing [11], at elevated temperatures >150 °C and pressures > 70 MPa [4]. The following study focuses on the light scattering experimental setup and validation experiments using small molecules, such that more complex fluids like, guar gum solutions and gels, may be studied.

1.2 Hydraulic Fracturing

Present-day hydraulic fracturing was preceded by stimulating oil wells with explosive “torpedos” [12]. Progress in the technology led to the first hydraulic fracturing experiment performed in Kansas in 1947 using gasoline thickened with napalm [10, 13]. Hydraulic fracturing is currently performed by drilling a vertical well followed by a horizontal well in a shale rich region [14, 15] as depicted in Figure 1.1. Initial fractures are made in the shale layer and propagated by a high-pressure fracturing fluid consisting of solvent, polymer, and proppant [10]. The fracturing fluid is degraded by a breaker so that hydrocarbons may be recovered. Fracturing fluids evolved to aqueous fluids composed of galactomannan biopolymer crosslinked to increase the viscoelasticity for supporting proppants and to prevent fluid leak off. Linear and borate crosslinked guar gum are the most commonly used fracturing fluids due to accessibility and cost efficiency as well as significant viscosity increases with low polymer loadings (< 1 wt%) [16, 10]. Borate crosslinked guar gum has also been shown to have a strongly pressure dependent viscosity [17]. In Figure 1.2, after the first 20 minutes of the experiment time, the pressure is increased stepwise to ~ 670 bar followed by a stepwise decrease in pressure. The corresponding viscosity values decrease with increased pressure and increase with decreased pressure. It is important to note that borate crosslinked guar

gum exhibits a recoverable pressure dependent viscosity.

The fracturing fluid components of interest to this work are guar gum biopolymer and borate crosslinker. The evolution of oil well fracturing from explosive devices to finely tuned complex fluids has greatly improved hydrocarbon recovery, but the high-pressure behavior of these fluids needs further characterization.

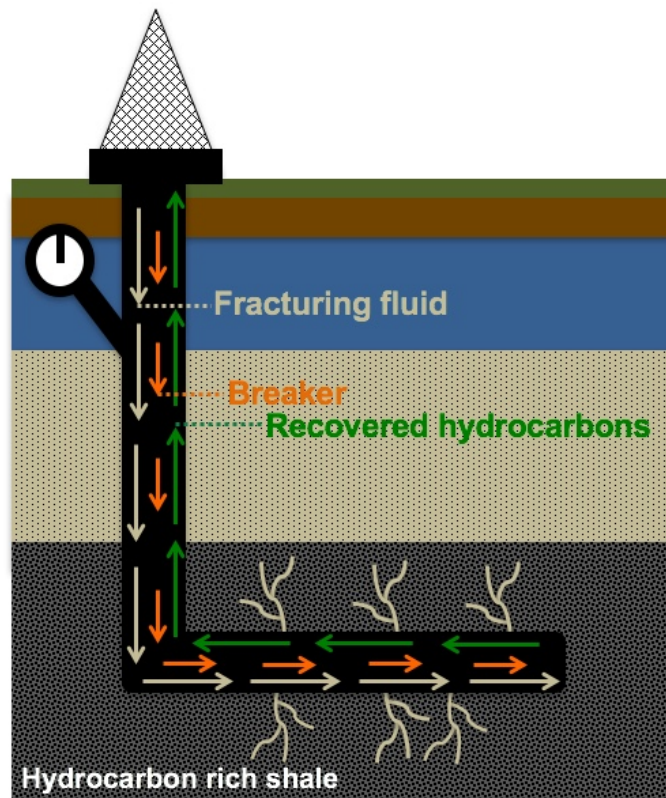


Figure 1.1: Simplified schematic of fracturing showing a vertical well expanded into a horizontal well. From the horizontal well, fractures in the subterranean hydrocarbon rich shale are visible.

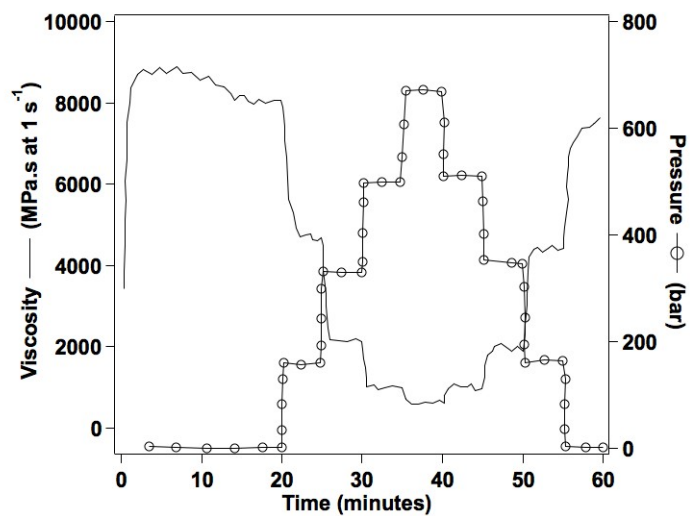


Figure 1.2: Pressure dependent viscosity of 0.3 wt% guar solution crosslinked with 60 ppm boron at 30°C and pH 9. Data taken from Parris et al. 2008 [17].

1.3 Microrheology

Rheometry is used to measure the viscoelastic nature of complex fluids, such as fracturing fluids, over a range of length and time scales. In particular, complex fluids have microstructures that affect their flow behavior over material length scales [18]. To study the viscoelasticity of complex fluids, both mechanical and microrheological techniques are employed. Mechanical rheometry is typically performed by applying a stress or strain and observing the material’s flow and deformation to obtain bulk viscosity and moduli. In contrast, microrheology uses the motion of colloidal probes to extract rheological behavior. These complimentary techniques aid in characterizing material behavior over a range of time and length scales. Microrheology is advantageous for this work due to the accessible pressure range and nondestructive nature of the technique.

Microrheology is divided into two categories, active and passive. Active microrheology probes are subjected to applied forces using, for instance, laser tweezers or magnetic tweezers. Passive microrheology uses the inherent thermal motion of probes, and includes techniques such as multiple particle tracking, dynamic light scattering (DLS), and diffusing wave spectroscopy (DWS) [18]. Passive microrheology techniques measure the displacement of particles, such as polystyrene microspheres or emulsion droplets, undergoing thermal fluctuations known as Brownian motion. Passive microrheology may be traced to Robert Brown’s experiments in 1828 [19], where he observed pollen organelle motion in water. In 1905, Einstein (and independently, Sutherland [20]) interpreted Brown’s observations in terms of the collision of particles with surrounding water molecules [21]. This thermal motion, referred to as Brownian motion, is characterized by the diffusion coefficient D and related to the hydrodynamic drag force ξ derived by George G. Stokes [22] by

$$D = \frac{k_B T}{\xi} \quad (1.1)$$

with Boltzmann constant k_B and temperature T . If the molecule is spherical, then ξ may be substituted for $6\pi\mu a$ and the relation is referred to as the Stokes-Einstein or

Stokes-Einstein-Sutherland equation

$$D = \frac{k_B T}{6\pi\mu a}. \quad (1.2)$$

with viscosity μ (sometimes, η) and probe particle radius a . The passive microrheology techniques used in this study include multiple particle tracking and diffusing wave spectroscopy.

1.4 Multiple Particle Tracking

Multiple particle tracking as described in literature [23] is possible through the use of a light microscope, high-speed camera, and computer with appropriate software uses a brightness-weighted centroid algorithm. Interactive Data Language (IDL) code from Crocker and Weeks [24] and Matlab routines from Blair, Defresne, and Kilfoil [25, 26] are available. The algorithm generates particle trajectories from an image stack.

1.5 Diffusing Wave Spectroscopy

Light scattering is sensitive to the small fluctuations of probe particles and thus extends the frequency range of passive techniques [18]. Dynamic light scattering and Diffusing wave spectroscopy are performed in the single and multiple scattering limits, respectively. A limitation of DLS is that it requires samples to only transmit singly-scattered light, which restricts the materials and concentrations to those that are not optically thick or opaque. DWS extends light scattering to turbid samples that only exhibit multiple light scattering. DWS provides information over a wide frequency range during a single experiment, gives information about the microstructure, and has been shown to agree with macroscopic measurements in many cases [18, 27]. Microrheological techniques, such as DWS, may be modified to study material properties at elevated temperatures and pressures. High-pressure DWS is advantageous for characterizing complex fluids due to solution-gel transition sensitivity and its nondestructive nature as demonstrated by studies of colloidal gelation [28] and block copolymer phase

transitions [8]. The following section is an overview of DWS as described in other texts [29, 27, 30, 31]. When an optically dense particle suspension is illuminated, the incident light penetrates a distance z_0 before scattering off particles in a random trajectory as shown in Figure 1.3, where scattering events are separated by a distance l and the photon direction is randomized after traveling the mean free path l^* . The propagation of light through the sample shares similarities with more typical transport phenomena, like heat or mass transfer, allowing the propagation to be approximated as photons of light diffusing through the sample. As particles move, fluctuations in the transmitted light occur due to constructive and destructive interference of the diffusing waves, which can be observed in a speckle pattern. The fluctuations are measured over delay time τ and converted into the intensity autocorrelation function

$$g_2(\tau) = \frac{\langle I(\tau_0)I(\tau_0 + \tau) \rangle}{\langle I^2 \rangle} \quad (1.3)$$

with initial delay time τ_0 , intensity I , and the ensemble average represented by angle brackets. The intensity autocorrelation function is converted into the electric field autocorrelation function $g_1(\tau)$ using the Siegert relation

$$g_2(\tau) = 1 + \beta |g_1(\tau)|^2 \quad (1.4)$$

with dynamical contrast β to account for noise in the intensity measurement.

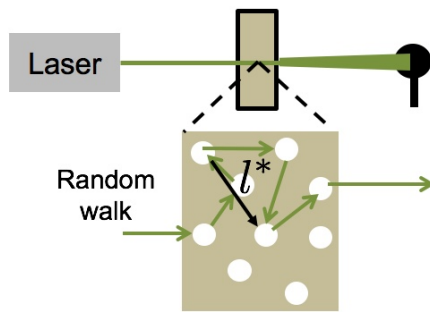


Figure 1.3: Schematic of photon propagation in point source illumination in the transmission geometry.

The intensity autocorrelation function provides information about the light scattered by the sample. The electric field autocorrelation function provides information about the particle movements which can be related to the mean square displacement $\langle \Delta r^2(\tau) \rangle$ using

$$g_1(\tau) = \int_0^\infty \mathcal{P}(s) \exp \left[\left(-\frac{s}{3l^*} \right) k_0^2 \langle \Delta r^2(\tau) \rangle \right] ds \quad (1.5)$$

with distribution of photon paths $\mathcal{P}(s)$, wavevector k_0 , and $s = c/\tau$, where c is the speed of light in the medium.

The mean free path is determined from Mie Scattering theory and is a weighted average of particle form factor $P(q)$ and structure factor $S(q)$,

$$l^* = k_0^{-6} \left(\pi \rho \int_0^{2k_0} P(q) S(q) q^3 dq \right)^{-1} \quad (1.6)$$

with scattering wavevector q and number density of scatterers ρ . The mean free path is a function of particle and sample refractive indices, probe volume fraction, particle size, and laser wavelength. A comparison of the scattering and mean free paths as a function of scaled particle size is shown in Figure 1.4. Larger particles ($ka \geq 1$) tend to scatter light in the forward direction while smaller particles ($ka \ll 1$) scatter light isotropically. For isotropic scattering, the photon mean free path scales with the scattering mean free path. As particle size increases, the mean free path becomes much larger than the scattering mean free path due to needing more scattering events to randomize the photon path.

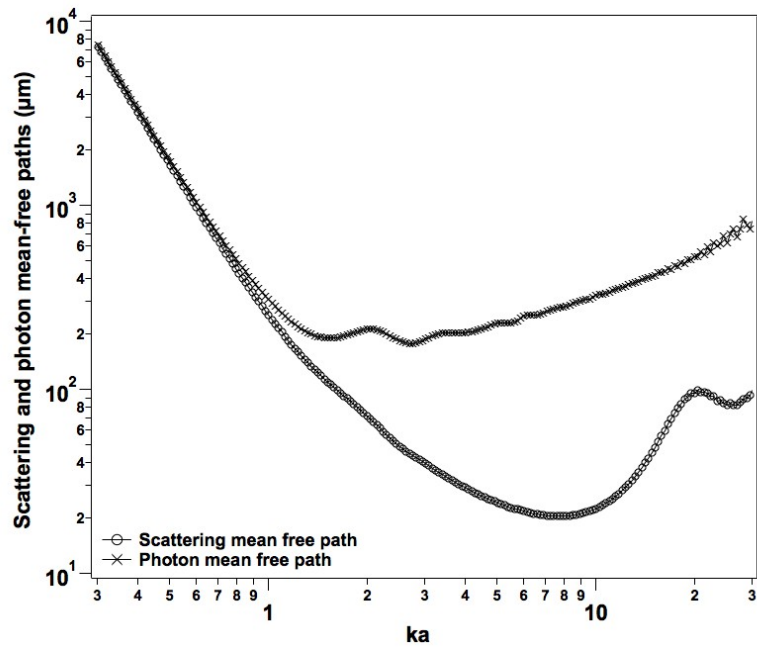


Figure 1.4: Scattering (l) and photon (l^*) mean free paths as a function of particle size (a) scaled by scattering wave vector (k) for hypothetical 1 vol% particle dispersion.

Diffusing wave spectroscopy is usually performed with either plane wave or point source illumination in transmission or backscattering geometries. An intermediate illumination method is a gaussian beam, where the beam diameter is considered. The illumination and geometry impacts the interpretation of the light scattering due to the effect on the photon path length distribution, $\mathcal{P}(s)$. Schematics of point source transmission and plane wave backscattering are shown in Figures 1.5 and 1.6. The illumination technique is changed from point source to plane wave by adding a beam expander. The geometry is determined by the orientation of the detector in reference to the incident beam and sample. The transmission geometry is used for light scattered through the sample while backscattering is used for light scattered from the incident plane [30].

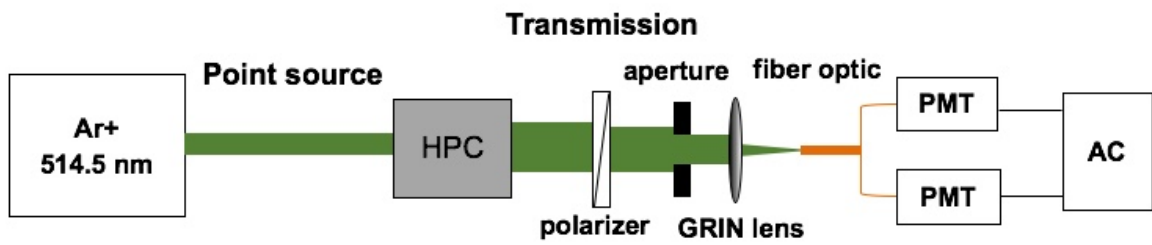


Figure 1.5: Schematic of point source illumination in the transmission geometry with gradient refractive index (GRIN) lens.

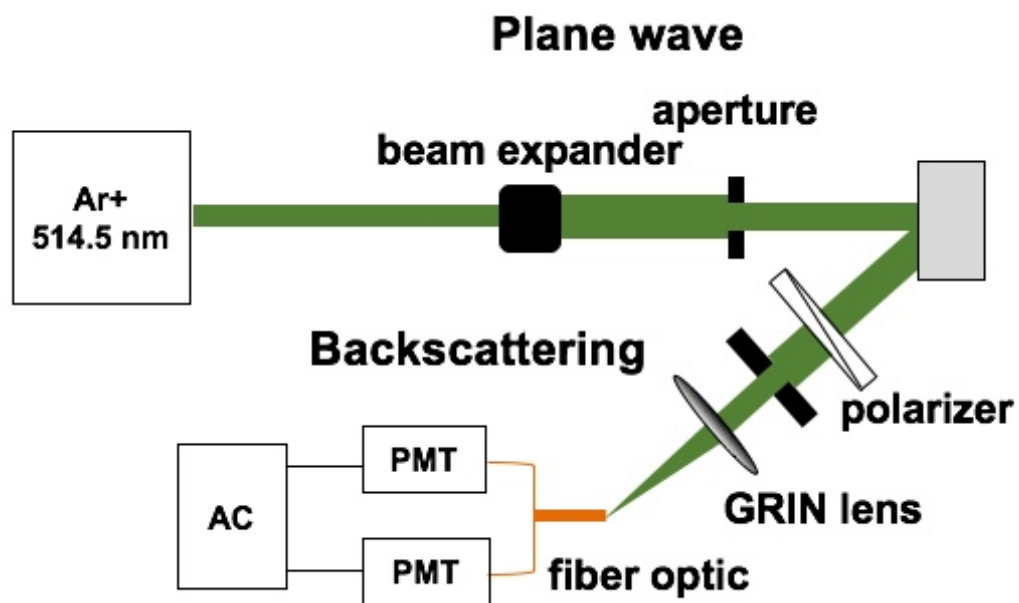


Figure 1.6: Schematic of plane wave illumination in the backscattering geometry.

After converting the intensity autocorrelation function to the electric field autocorrelation function, the mean square displacement may be determined by using the appropriate equation. For plane wave transmission, the photon diffusion is treated as one-dimensional and is analogous to steady state heat transfer due to an instantaneous planar source [31]. The field autocorrelation function is

$$g_{(1)}(\tau) = \frac{\frac{L/l^*+4/3}{z_0/l^*+2/3} \left\{ \sinh \left[\frac{z_0}{l^*} R(\tau) \right] + \frac{2}{3} R(\tau) \cosh \left[\frac{z_0}{l^*} R(\tau) \right] \right\}}{\left(1 + \frac{4}{9} R^2(\tau) \right) \sinh \left[\frac{L}{l^*} R(\tau) \right] + \frac{4}{3} R(\tau) \cosh \left[\frac{L}{l^*} R(\tau) \right]}. \quad (1.7)$$

The explicit expression for DWS performed with point source illumination in transmission mode is [30],

$$g_1(\tau) = \frac{\int_{(L/l^*)R(\tau)}^{\infty} \left[A(y) \sinh(y) + e^{-y(1-z_0/L)} \right] dy}{\int_0^{\infty} \left[A(y) \sinh(y) + e^{-y(1-z_0/L)} \right] dy} \quad (1.8)$$

with

$$(L/l^*)R(\tau) = (L/l^*) \sqrt{(k_0^2 < \Delta r^2(\tau) >)} \quad (1.9)$$

and

$$A(y) = \frac{(\epsilon y - 1) [\epsilon y e^{-yz_0/L} + (\sinh(y) + \epsilon y \cosh(y)) e^{-y(1-z_0/L)}]}{(\sinh(y) + \epsilon y \cosh(y))^2 - (\epsilon y)^2} \quad (1.10)$$

with

$$\epsilon = 2l^*/3L. \quad (1.11)$$

The gaussian beam equations are as follows [31]

$$g_1(\tau) = C' \int_{(L/l^*)R(\tau)}^{\infty} e^{-(\xi^2 - (L/l^*R(\tau)))^2 (\delta/4)^2} D(\xi, \epsilon, \zeta) \xi e^{(-1+\zeta)\xi} d\xi \quad (1.12)$$

with

$$D(\xi, \epsilon, \zeta) = \frac{2\epsilon \left[((1 + \epsilon\xi) - (1 - \epsilon\xi)e^{-2\zeta\xi}) \right]}{(1 + \epsilon\xi)^2 - (1 - \epsilon\xi)^2 e^{-2\zeta\xi}} \quad (1.13)$$

with integration variable ξ , $\zeta = z_0/L$, $\delta = d/L$ where d is beam diameter, and normalization constant C' .

For backscattering experiments, the beam is typically expanded such that an area of the incident face is uniformly illuminated to a value much greater than l^* [31]

$$g_{(1)}(\tau) = \frac{\sinh[R(t) \left(\frac{L}{l^*} - \frac{z_0}{l^*} \right)] + \frac{2}{3} R(t) \cosh[R(t) \left(\frac{L}{l^*} - \frac{z_0}{l^*} \right)]}{\left(1 + \frac{4}{9} R^2(t) \right) \sinh \left[\frac{L}{l^*} R(t) \right] + \frac{4}{3} R(t) \cosh \left[\frac{L}{l^*} R(t) \right]} \quad (1.14)$$

Here, we use the transmission geometry. The characteristic behavior of the transmission intensity and electric field autocorrelation functions is shown in Figures 1.7 and 1.8. Values for l^* were calculated using Mie theory for 0.6, 1.1, and 2.2 μm diameter polystyrene spheres at 1 and 2 vol% by Lu and Solomon[32]. Graphing the correlation function on a log-linear plot at short delay times, there is an initial plateau that decays at intermediate delay times before plateauing again at long delay times. At short delay times the plot may be interpreted as the laser light intensity being correlated because the particles have not moved far enough to cause a decorrelation. At intermediate delay times, the decay is attributed to particle diffusion and at long delay times the particles have moved far enough that the light fluctuations are no longer correlated.

Figure 1.7 shows the change in $g_2(\tau) - 1$ with plane, point, and gaussian transmission geometries as a function of l^* . For the transmission geometry, the onset of decay occurs first for plane wave and last for point source with the gaussian beam in the middle. The difference is due to the weighting of long and short photon paths. Longer photon paths dominate plane wave and transmission geometries, and shorter photon paths dominate point source and backscattering geometries. Shifts in the autocorrelation functions also occur with changing the l^* value. An increase in l^* corresponds to an increase in the distance to randomize the photon path and increases the decay onset. The shift to earlier decay times with increasing sample pathlength is shown in Figure 1.9. Increasing the pathlength results in stronger weighting of longer photon pathlengths, which shifts the autocorrelation function to shorter delay times.

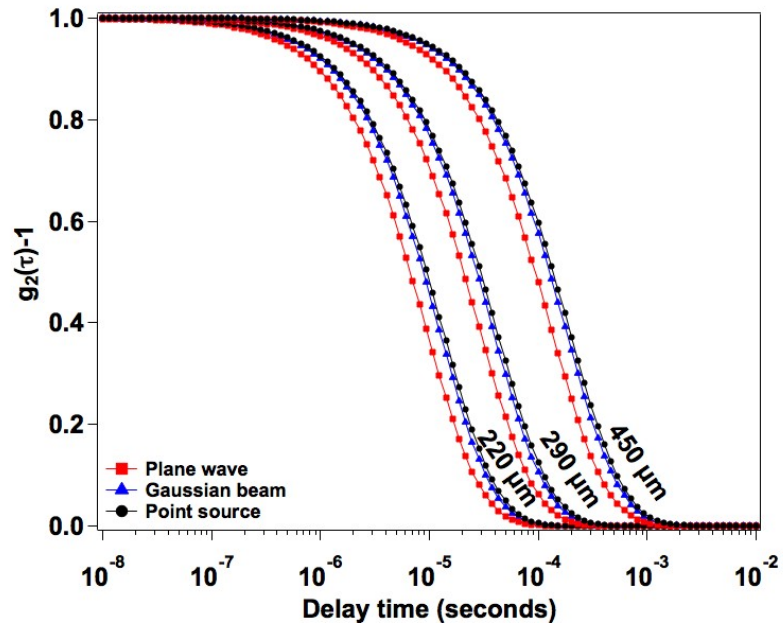


Figure 1.7: Theoretical $g_2(\tau) - 1$ as a function of delay time for point source, plane wave, and gaussian beam with $l^* = 220, 290,$ and $450 \mu\text{m}$. The hypothetical samples correspond to 1 vol% aqueous dispersions of 0.6, 1.1, and $2.2 \mu\text{m}$ diameter polystyrene microspheres in a 4.5 mm cuvette at 20°C .

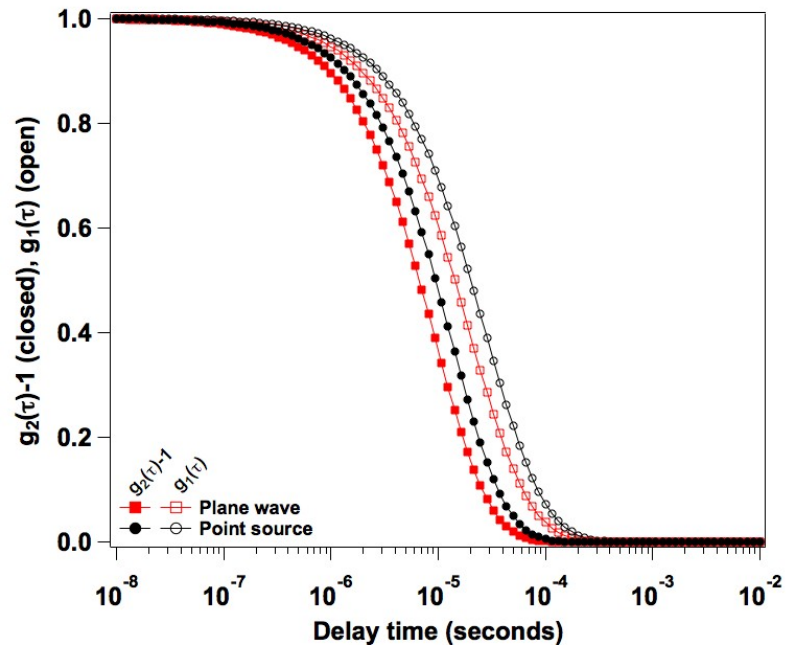


Figure 1.8: Theoretical $g_2(\tau) - 1$ and $g_1(\tau)$ as a function of delay time for point source and plane wave with $l^* = 220 \mu\text{m}$. The hypothetical sample corresponds to a 1 vol% aqueous dispersion of $1.1 \mu\text{m}$ diameter polystyrene microspheres in a 4.5 mm cuvette at $20 \text{ }^\circ\text{C}$.

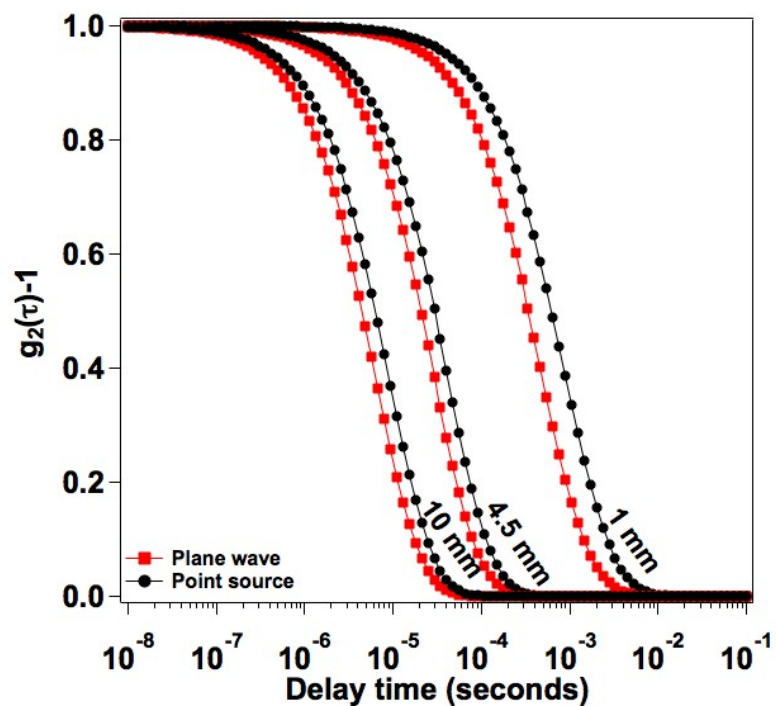


Figure 1.9: Theoretical $g_2(\tau) - 1$ as a function of delay time for point source and plane wave with $l^* = 290 \mu\text{m}$ for $1.1 \mu\text{m}$ diameter polystyrene dispersion in water for 1, 4.5, and 10 mm pathlengths at 20°C .

REFERENCES

- [1] A. Aertsen, F. Meersman, M. E. Hendrickx, R. F. Vogel, and C. W. Michiels. Biotechnology under high pressure: applications and implications. *Trends in Biotechnology*, 27(7):434–441, 2009.
- [2] F. Abe and K. Horikoshi. The biotechnological potential of piezophiles. *Trends in Biotechnology*, 19(3):102–108, 2001.
- [3] N. K. Rastogi, K. S. M. S. Raghavarao, V. M. Balasubramaniam, K. Niranjana, and D. Knorr. Opportunities and challenges in high pressure processing of foods. *Critical Reviews in Food Science and Nutrition*, 47(1):69–112, 2007.
- [4] G. DeBruijn, C. Skeates, R. Greenaway, D. Harrison, M. Parris, S. James, F. Mueller, S. Ray, M. Riding, L. Temple, and K. Wutherich. High-pressure, high-temperature technologies. *Oilfield Review*, 20(3):46–60, 2008.
- [5] F. J. M. Boza and C. Gallegos. *Rheology: High Pressure Rheology*. EOLSS Publishers, 2010.
- [6] Y. Y. Hou and H. O. Kassim. Instrument techniques for rheometry. *Review of Scientific Instruments*, 76:101101, 2005.
- [7] Discovery hybrid rheometer. URL http://www.tainstruments.com/wp-content/uploads/dhr_brochure.pdf.
- [8] C. J. Kloxin and J. H. van Zanten. High pressure phase diagram of an aqueous PEO-PPO-PEO triblock copolymer system via probe diffusion measurements. *Macromolecules*, 43(4):2084–2087, 2010.

- [9] N. Thombare, U. Jha, S. Mishra, and M. Siddiqui. Guar gum as a promising starting material for diverse applications: A review. *International Journal of Biological Macromolecules*, 88:361–372, 2016.
- [10] R. Barati and J. Liang. A review of fracturing fluid systems used for hydraulic fracturing of oil and gas wells. *Journal of Applied Polymer Science*, 131(16):40735, 2014.
- [11] S. Wang, Y. Zhang, J. Guo, J. Lai, D. Wang, L. He, and Y. Qin. A study of relation between suspension behavior and microstructure and viscoelastic property of guar gum fracturing fluid. *Journal of Petroleum Science and Engineering*, 124:432–435, 2014.
- [12] E. A. Roberts. U.S. patent 59936A issued November 20, 1866. URL <https://www.google.com/patents/US59936>.
- [13] S. A. Holditch. Hydraulic fracturing: Overview, trends, issues. *Drilling Contractor*, 2007.
- [14] The process of unconventional natural gas production. URL <https://www.epa.gov/hydraulicfracturing/process-hydraulic-fracturing>.
- [15] Explore shale. Online, 2014. URL <http://exploreshale.org/>.
- [16] L. Li, G. A. Al-Muntasheri, and F. Liang. A review of crosslinked fracturing fluids prepared with produced water. *Petroleum*, 2(4):313–323, 2016.
- [17] M. D. Parris, B. A. MacKay, J. W. Rathke, R. J. Klingler, and R. E. Gerald II. Influence of pressure on boron cross-linked polymer gels. *Macromolecules*, 41(21):8181–8186, 2008.
- [18] T. A. Waigh. Microrheology of complex fluids. *Reports on Progress in Physics*, 68:685–742, 2005.

- [19] R. Brown. A brief account of microscopical observations made in the months of June, July, and August 1827, on the particles contained in the pollen of plants; and on the general existence of active molecules in organic and inorganic bodies. *The Philosophical Magazine and Annals of Philosophy*, 4(21):161–173, 1828.
- [20] W. Sutherland. A dynamical theory of diffusion for non-electrolytes and the molecular mass of albumin. *Philosophical Magazine Series 6*, 9(54):781–785, 1905.
- [21] A. Einstein. On the movement of small particles suspended in stationary liquids required by the molecular-kinetic theory of heat (Über die von der molekularkinetischen theorie der wärme geforderte bewegung von in ruhenden flüssigkeiten suspendierten teilchen). *Annalen der Physik*, 322(8):549–560, 1905.
- [22] G. G. Stokes. On the effect of the internal friction of fluids on the motion of pendulums. *Transactions of the Cambridge Philosophical Society*, 9:8, 1850.
- [23] J. C. Crocker and D. G. Grier. Methods of digital video microscopy for colloidal studies. *Journal of Colloid and Interface Science*, 179:298–310, 1996.
- [24] J. C. Crocker and E. R. Weeks. Particle tracking using IDL. URL <http://www.physics.emory.edu/faculty/weeks//idl/>.
- [25] D. Blair and E. Dufresne. The matlab particle tracking code repository. URL <http://site.physics.georgetown.edu/matlab/>.
- [26] M. Kilfoil. Software tools. URL <http://people.umass.edu/kilfoil/tools.php>.
- [27] T. G. Mason and D. A. Weitz. Optical measurements of frequency-dependent linear viscoelastic moduli of complex fluids. *Physical Review Letters*, 74(7):1250–1253, 1995.
- [28] R. Vavrin, J. Kohlbrecher, A. Wilk, M. Ratajczyk, M. P. Lettinga, J. Buitenhuis, and G. Meier. Structure and phase diagram of an adhesive colloidal dispersion

- under high pressure: A small angle neutron scattering, diffusing wave spectroscopy, and light scattering study. *The Journal of Chemical Physics*, 130:154903, 2009.
- [29] E. M. Furst and T. M. Squires. *Microrheology*. Oxford University Press, 2017.
- [30] D. J. Pine, D. A. Weitz, J. X. Zhu, and E. Herbolzheimer. Diffusing-wave spectroscopy: dynamic light scattering in the multiple scattering limit. *Journal de Physique*, 51(18):2101–2127, 1990.
- [31] D. A. Weitz and D. J. Pine. *Dynamic Light Scattering: Diffusing-wave spectroscopy*. Ed. W. Brown. Oxford University Press Inc., 1993.
- [32] Q. Lu and M. J. Solomon. Probe size effects on the microrheology of associating polymer solutions. *Physical Review E*, 66(6):061504, 2002.

Chapter 2

MATERIALS AND METHODS

The following section describes the materials and techniques used for microrheology, mechanical rheometry, and high-pressure diffusing wave spectroscopy. Microrheology and mechanical rheometry are used as complimentary techniques to determine rheological properties at ambient conditions. High-pressure microrheology is used to assess high-pressure, high-frequency rheology. Microrheology was performed with washed micrometer-diameter polystyrene spheres. High-purity 1-propanol was used in an aqueous mixture for validating the high-pressure cell. Poly(ethylene oxide) was used as a model viscoelastic fluid. Guar gum biopolymer was processed to remove impurities [1, 2, 3], improve reproducibility, and prevent over-crosslinking with borate.

2.1 Materials

Polystyrene spheres (1.04 μm , 5% w/v, Spherotech) were embedded as probe particles into samples for light scattering measurements. The probes were washed 3 times by centrifugation (Centrifuge 5424, Eppendorf) at 6,000 rpm for 5 minutes followed by replacing 200 μL of the supernatant with ultrapure water (Milli-Q, 18.2 $\text{M}\Omega\cdot\text{cm}$). The process was repeated 3 times to remove impurities. For high-pressure validation, 1-propanol (HPLC grade, Sigma Aldrich) was used. Poly(ethylene oxide) (PEO, $M_v \sim 200$ kDa, Sigma Aldrich) was used as a model viscoelastic fluid. PEO samples were prepared by heating in a 60 $^\circ\text{C}$ oven with periodic magnetic stirring over 5 days.

Guar gum (Schlumberger) was purified following a modified procedure [4] to removed impurities and improve reproducibility. A 1 wt% guar gum solution is magnetically stirred for 5 hours. The readily hydrated guar is separated from any insoluble

clumps and then centrifuged for 1 hour at 4,000 rpm (Centrifuge 5810 R, Eppendorf). The supernatant containing guar gum is decanted leaving a pellet of impurities and less hydrophilic guar gum. The supernatant is precipitated with a half volume of acetone and then centrifuged again at 4,000 rpm for 30 minutes. The supernatant containing water and acetone is removed leaving a pellet of guar gum. The pellet is frozen in liquid nitrogen for 1-2 minutes and then lyophilized (Millrock Technology) until dry. The dried pellet is then cryo-milled with liquid nitrogen to produce a powder that is readily hydrated in water.

Guar gum solutions were prepared by adding the desired amount of polymer to magnetically stirring ultrapure water in a 100 mL vial. The solutions were then high-shear mixed (L4RT, Silverson) at 2,000 rpm with periodic hand mixing until a visibly homogeneous solution was made. Polymer concentration was verified with triplicate runs by drying the samples in a moisture analyzer (HR73 Halogen Moisture Analyze, Mettler Toledo). Guar gum solutions were crosslinked with borate ions from sodium tetraborate decahydrate (ACS Reagent, $\geq 99.5\%$, Sigma Aldrich). The pH of the desired amount of guar gum was determined using a pH meter (AB15, Fisher Scientific). The guar gum solution was acidified using a few drops of 0.05 M HCl to pH 4-6 before borate solution was added. After adding borate, the pH recovered to pH 8-9, which is in the crosslinkable range [5]. The borate and guar gum solutions were magnetically stirred for an additional minute after reaching the crosslinkable pH. As the system continued mixing, the stir bar slowed down, indicating an increase in the viscoelastic properties consistent with crosslinking.

2.2 Multiple Particle Tracking

Samples are loaded into 50 mm borosilicate tubing (VitroCom) by capillary action and affixed to microscope slides with optical adhesive (NOA 81, Norland Optical Adhesive). Fluorescent probe particles (1.0 μm , Life Technologies) are imaged with a 40x objective (EX Plan-Neofluar, NA 0.75, Carl Zeiss) and an inverted microscope (Axiovert 200, Carl Zeiss). A high-speed camera (Phantom v5.1, 1024 pixels, Vision

Research, Wayne, NJ) is used to record videos of the particles at an acquisition rate of 30 frames per second. A brightness-weighted centroid algorithm is used to track probe positions, which are linked together in consecutive video frames to produce trajectories.

2.3 Diffusing Wave Spectroscopy

The DWS setup is operated in transmission mode with point source illumination. An argon ion laser (Innova 90C-5) operating with a wavelength of 514.5 nm and vertical polarization illuminates the sample. The multiply-scattered light is collected in a gradient refractive index (GRIN) lens collimated to a single mode fiber optic. The signal is split into 2 photomultiplier tubes (Brookhaven BI-CCDS) and the cross-correlation is taken by an autocorrelator (Brookhaven BI-9000AT).

2.4 Density Measurements

The composition of stock aqueous polystyrene suspensions were characterized by measuring solution density with a densimeter (DDM 2911 Plus, Automatic Density Meter, Rudolph Research Analytical). Assuming no interactions between polystyrene and water, the composition x of polystyrene was determined using the equation below.

$$(x)\rho_{\text{PS}} + (1 - x)\rho_{\text{W}} = \rho_{\text{S}} \quad (2.1)$$

with density of polystyrene ρ_{PS} , water ρ_{W} , and suspension ρ_{S} .

2.5 Refractometry

The refractive index change with sample composition was determined using a refractometer (Rudolph Research, J157 Automatic Refractometer) operating at 658 nm. Due to the difference in wavelength of the refractometer and argon laser, these values were used as estimates.

2.6 Mechanical Rheology

Mechanical rheology measurements were performed on an AR-G2 rheometer with 60 mm, 2° and 40 mm, 4° cones and peltier plate. The preshear consisted of a

peak hold at 21 °C at 10 s⁻¹. An amplitude sweep was performed at 1 rad/s and 21 °C from 0.01-1000 strain %.

2.7 High-pressure Diffusing Wave Spectroscopy

The following section provides high-pressure cell specifications as well as design and experimental considerations. The initial high-pressure cell and system were modified to correct for leaks and improper pressurization. To properly account for the light transport as a function of pressure, the experimental effects of probe particles under pressure are assessed. While the sapphire windows permit sample illumination at elevated pressures, the effect of slight birefringence is considered.

2.7.1 High-pressure Cell and System Design

For high-pressure measurements, a high-pressure cell (HPC, Inconcel 718) with two sapphire windows (40-20 polish faces, 19.1 mm diameter × 19.1 mm thick, GT Advanced Technologies) was fabricated and used with a high-pressure system (316 stainless steel, High Pressure Equipment Co.) with a low pressure gauge (34.5 MPa, ±0.5%, High Pressure Equipment Co.) and high pressure gauges (344.74 MPa, ±0.5%, High Pressure Equipment Co.). The high-pressure cell is operable up to 207 MPa and 300 °C. The sapphire windows permit light to enter and exit the high-pressure cell. A schematic of the high-pressure cell is shown in Figure 2.1. The pathlength is 11.8 mm and internal sample volume is 4 mL. The high-pressure cell is connected to a high-pressure system as shown in Figure 2.2. Images of the experimental system, assembled high-pressure cell, and sapphire windows are shown in Figures 2.4, 2.4, and 2.5. The high-pressure generator is rated to 207 MPa and sets the pressure limit of the system. Valves allow or restrict access to the low-pressure gauge, reservoir, and piston.

During operation, the working fluid, ultrapure water, is drawn into the pressure generator from the reservoir by turning the pressure generator handles counterclockwise while only the reservoir valve is opened. The reservoir valve is closed before the valve to the piston is opened. The valve to the low pressure gauge is opened only if the

desired operating pressure is less than 31 MPa. If the desired pressure is 32-200 MPa, then the low pressure gauge valve remains closed. The pressure generator handles are turned clockwise to compress the working fluid and pressurize the system. If the desired pressure is not achieved with a single stroke, then the valve to the piston and high-pressure cell is closed and the pressure is noted. The pressure generator handles are turned counterclockwise to removed the pressure. The reservoir valve is opened and additional working fluid is drawn into the pressure generator. The reservoir valve is closed and the pressure generator is compressed until the previously noted pressure is achieved. The valve to the piston and high-pressure cell is opened and the entire system is pressurized until the desired pressure is achieved or another stroke of the generator is complete.

The volume change with pressure at constant temperature can be determined using

$$\frac{V_2}{V_1} = \exp\left(\frac{P_1 - P_2}{\kappa}\right) \quad (2.2)$$

with volume V , pressure P , and bulk modulus κ .

The cylindrical piston body is 15.24 cm long with a diameter of 1.12 cm. The total volume of the piston body (less the piston) is 12.5 mL. The piston is inserted such that the sample volume and working fluid volumes are approximately 9 mL and 3 mL, respectively. In Table 2.1, the volume change for 15 mL of pure water and air are estimated as a function of pressure using the bulk modulus. The volume change for air is larger than the volume change allowed by the experimental setup, so the piston displacement is not applicable (N/A).

Substance	V_1 (mL)	P_1 (Pa)	P_2 (Pa)	κ_{STP} (Pa)	V_2 (mL)	Piston displacement (cm)
Water	15	101,352.9	2.07×10^8	2.07×10^8	13.65	1.37
Air	15	101,352.9	374,865.9	1.01×10^5	1	N/A

Table 2.1: Volume change with increase in pressure

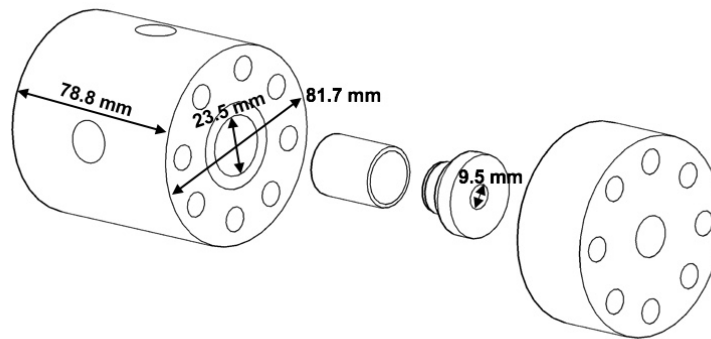


Figure 2.1: High-pressure cell schematic with cell body length and inner and outer diameters.

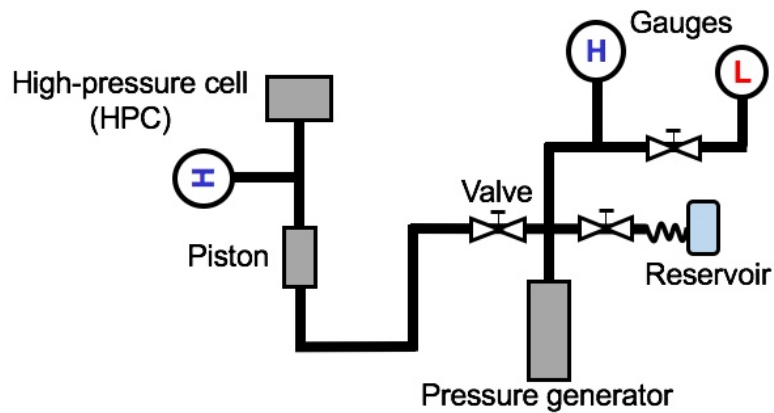


Figure 2.2: Schematic of high-pressure system setup.

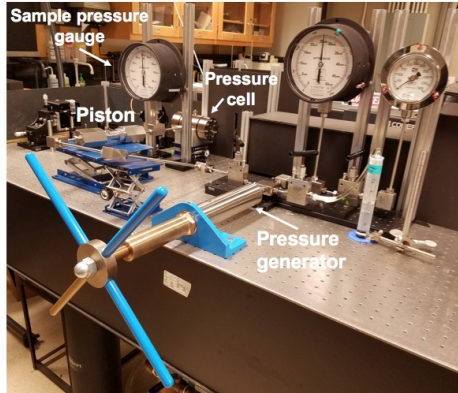


Figure 2.3: Image of the high-pressure system and cell integrated into a light scattering setup.

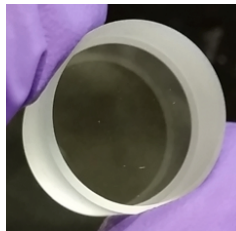


Figure 2.4: Image of cylindrical sapphire window used to permit light scattering through the cell at elevated pressures.



Figure 2.5: Assembled high-pressure cell resting in aluminum jaws. Side left connection goes to sample gauge and piston. Top port is shown with plug.

During an experiment, the pressure of the working fluid and sample are the same. However, piston jamming and bottoming out may prevent the sample side from reaching the working fluid pressure. Piston jamming occurred and was attributed to non-uniformity in the thickness of the piston. Trimming the as-received pistons to a tighter diameter specification improved loading and prevented jamming. During pressurization, excess displacement of the piston may cause bottoming out, which results in deformation of the piston as shown in Figure 2.6. This deformation prevents the piston from being reused as causes scarring on the inner cylinder of the piston body. To prevent this deformation, hardened pistons were used. To ensure that the sample is pressurized to the working fluid pressure, a method for directly or indirectly tracking the piston should be used. In this work, a gauge is added to the sample side to verify experimental pressures and indirectly determine relative piston position. In contrast, a linear variable differential transformer (LVDT) may be added to directly assess piston position [6]. It is also essential to prevent leaks. Two regions that are prone to leaks are the seal between the sapphire window and window cap and the mating surfaces between the window cap holder and the high-pressure cell. The seal between the sapphire window and the sapphire window holder is maintained by a polyimide film o-ring (Kapton[®], DuPont[™]). These o-rings are made by punching out disks from a sheet using sharpened punches (Anytime Tools). The disk is made to have a 0.5 in inner diameter and 0.75 in outer diameter as shown in Figure 2.7. Dull punches may result in rough edges and cause leaks. The sapphire window holder caps include a lip above the threads, which allows for extra hand torquing to compress the o-ring and form the seal between the cap and window. High-purity nitrogen is blown over all surfaces to remove any particulate matter that may prevent a proper seal and cause leaks. Pressure validation is shown in Figure 2.8, where the system settled to 197 MPa over time. System relaxation is expected and may result in leaks if the system is pressurized too quickly.



Figure 2.6: Piston with (right) and without deformation (left) caused by bottoming out.

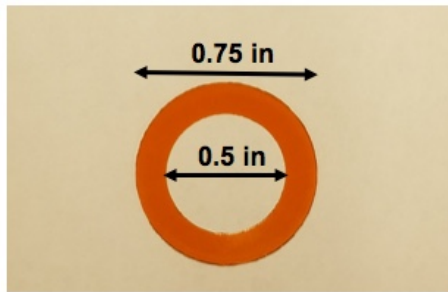


Figure 2.7: Image of one fabricated polyimide o-ring with inner and outer diameter dimensions.

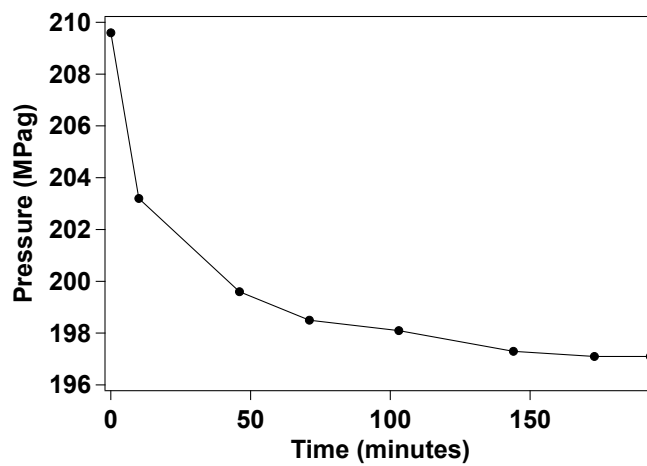


Figure 2.8: High-pressure cell pressure validation. The system was initially pressurized to 210 MPa and relaxed over time to 197 MPa.

Another key concern is air. Air is compressible and bubbles can interfere with light scattering. To prevent bubbles from being introduced into samples, the probe particles are mixed by inversion rather than vortex mixing. Any remaining bubbles may be removed by degassing. Proper care is required for sample loading to prevent the reintroduction of bubbles. The sample is loaded into the piston and high-pressure cell individually with a syringe and needle. Sample must be loaded into the piston to prevent the piston from prematurely bottoming out. The top port (Figure 2.5) of the high-pressure cell facilitates sample loading and bubble removal. Once the system is connected, the sample is compressed forward by the piston to fill the tubing and tee connector until sample is visible from the top port. After sealing the top port, the piston is compressed again to remove air from the sample pressure gauge tubing.

High-pressure work introduces physical hazards that must be addressed in a standard operating procedure (SOP). The principal physical hazards include high-pressurized release of water and sample from the system and equipment recoil. The experiment must be performed in a space equipped to handle a high-pressure release. To bolster the experimental space, polycarbonate shields (LexanTM) may be implemented to protect people and equipment in the event of system failure. Users should also be aware of the weight of system components as well as possible pinch points.

2.7.2 Key Considerations

At elevated pressures, special windows are required to permit light scattering, but there is a trade off between pressure resistance and optical properties. Sapphire windows have previously been used for light scattering [7, 8, 9]. However, birefringence may occur if the incident light is not on axis with the sapphire. Another consideration is probe particle compressibility. Decrease in the probe particle size may affect the light transport by increasing l^* as well as the hydrodynamic drag. These changes could be mistaken for changes in the rheology of the material under test.

Birefringence describes the change in refractive index due to incident light interacting with different planes. When incident light passes through a birefringent

material, the light is split into an ordinary-ray (o-ray) and extraordinary-ray (e-ray), which may result in wave interference. The difference between the refractive indices along the o-ray and e-ray is used to quantify birefringence. Sapphire is a uniaxial crystal and has a negative birefringence of -0.008 in the ultraviolet region due to larger o-ray refractive index [10]. To assess the effect of sapphire birefringence, an experiment was performed with 0.5 vol% aqueous polystyrene beads in 4.5 mm cuvette as shown in Figure 2.9. One and two sapphire windows were placed in the beam path. The initial position of the window was referred to as 0° and the windows were rotated from 0° to 90° . The normalized intensity autocorrelation functions for 5 configurations are shown in Figure 2.10. The functions overlap suggesting that birefringence does not significantly affect the light transport.

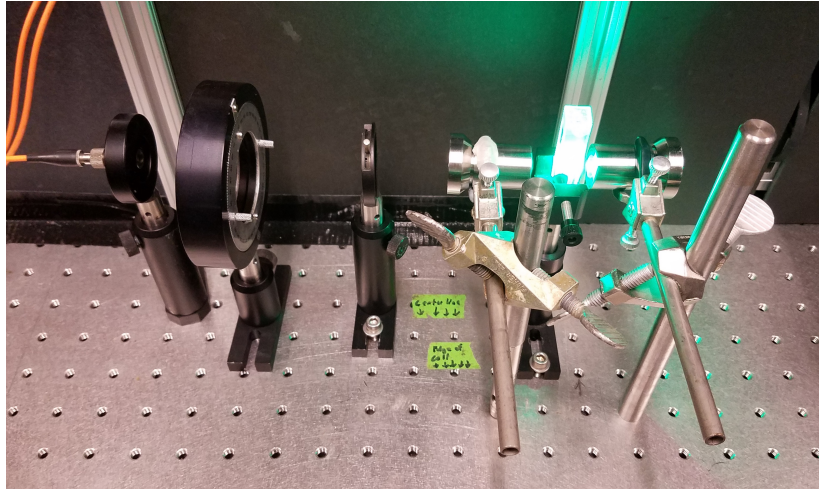


Figure 2.9: Experimental setup to assess effect of birefringence. In the laser beam path, a 4.5 mm cuvette is shown between 2 sapphire windows.

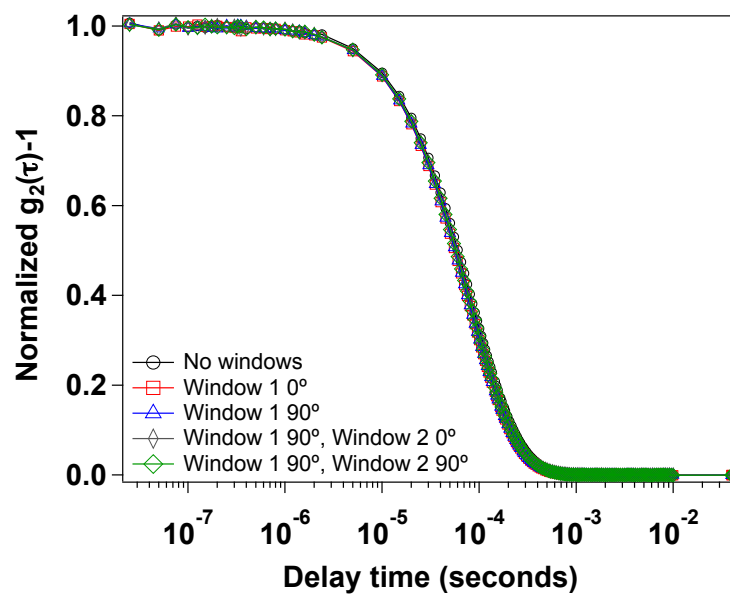


Figure 2.10: Normalized $g_2(\tau) - 1$ for 5 window setups with 0.5 vol% polystyrene in water in a 4.5 mm cuvette.

To accurately perform high-pressure microrheology, the probe particle containing sample must be tuned to ensure stability over the experimental range. Polystyrene probe particles are commonly used for DWS [11, 12, 13]. Previous workers found that over the range 0.1-28 MPa and 25-200°C, 204 nm polystyrene probes remained stable, however, at 300 °C, there was a change in colloidal stability that may be due to swelling [14]. Later studies at higher pressures up to 240 MPa found that l^* for 420 nm polystyrene spheres in water decreased from 213 nm at 20 °C and 0 MPa to 207 nm at 80 °C and 240 MPa resulting in a minor systematic error [7]. In addition, the changes in light transport and hydrodynamic size due to the compressibility of polystyrene must be separated from changes in rheological properties. As pressure is increased, the l^* value may increase corresponding to the change in volume percent of probe. The change in probe volume may be estimated using the following equations [15] with bulk polystyrene compressibility κ of $220 \times 10^{-6} \text{MPa}^{-1}$ [16].

$$\kappa = -\frac{1}{V} \left(\frac{dV}{dP} \right) \quad (2.3)$$

integrated

$$\frac{V_2}{V_1} = e^{-\kappa(P_2-P_1)} \quad (2.4)$$

with probe volume V and pressure P . The decrease in a $1 \mu\text{m}$ polystyrene particle volume is $0.023 \mu\text{m}^3$ for a change in pressure from atmospheric (0.1 MPa) to 206 MPa. The probe radius would decrease from $0.50 \mu\text{m}$ to $0.49 \mu\text{m}$. Assuming that no changes in the sample fluid refractive index occur, the change in probe volume results in change in l^* from $260 \mu\text{m}$ to $280 \mu\text{m}$ over the pressure range of interest. The expected (and small) change in intensity autocorrelation function is shown in Figure 2.11.

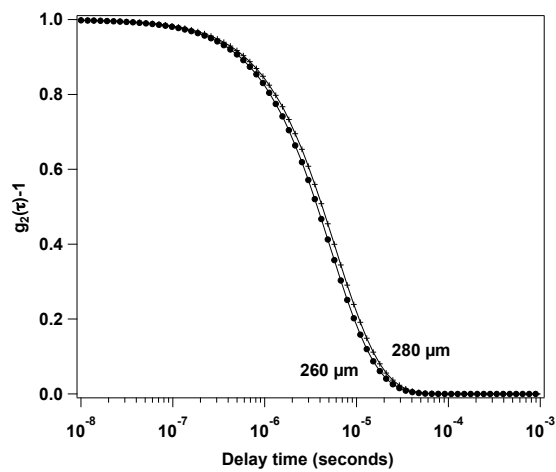


Figure 2.11: The hypothetical $g_2(\tau) - 1$ for $1 \mu\text{m}$ polystyrene particle dispersion with an 11.8 mm pathlength at atmospheric (0.1 MPa , $260 \mu\text{m}$) and elevated pressures (206 MPa , $280 \mu\text{m}$).

2.7.3 Operating Regime

A significant advantage of DWS is that small probe particle displacements may be captured. The corresponding short motion time scales allow for high-frequency material responses to be determined. The operating regime may be determined from the purely viscous and purely elastic limits [17] using the following equations,

$$\langle \Delta r^2(\tau) \rangle = \frac{k_b T \tau_{\min}}{6\pi a \eta_{\max}} \quad (2.5)$$

$$G \approx \frac{k_b T}{6\pi a \langle \Delta r^2(\tau) \rangle} \quad (2.6)$$

with shear modulus G . The transmission operating regime is shown in Figure 2.12. However, sample loading into the high-pressure cell further restricts the operating regime. Preliminary work with guar gum is discussed further in Section 4.2.

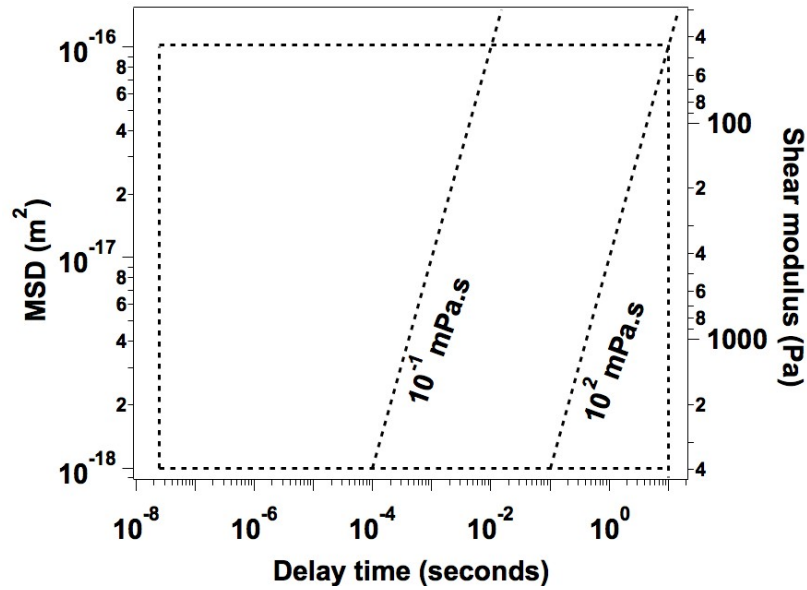


Figure 2.12: Transmission DWS operating regime for 0.5 vol% $1\mu\text{m}$ polystyrene beads in 11.8 mm pathlength at 25°C .

2.8 Purely Viscous Samples Data Analysis

To assess the relative effect of gravitational sedimentation to Brownian diffusion of the particles, the gravitational Péclet Pe_g number is used [18],

$$Pe_g = \frac{t_b}{t_g} = \frac{4\pi\Delta\rho a^4 g}{3k_b T}. \quad (2.7)$$

If $Pe_g \ll 1$, then Brownian motion dominates and if $Pe_g \gg 1$, then sedimentation dominates. In Table 2.2, using 1.05 g/mL as the density of polystyrene spheres, $Pe_g \ll 1$ indicating that Brownian motion dominates.

Component	ρ (g/mL), 25°C	Pe_g
Water	0.997	6.2×10^{-4}
1-propanol	0.804	2.9×10^{-3}

Table 2.2: Gravitational Péclet Pe_g for water and 1-propanol with 1 μm polystyrene spheres.

A sample of 1.05 vol% polystyrene probes in water in a 4.5 mm cuvette was analyzed in plane wave and point source transmission mode to test the data fitting procedure. Polystyrene probes were concentrated from 5 to 10 w/v% and the final concentration was determined using a densimeter. The l^* value was calculated from Mie theory to be 254 μm . However, the l^* for DWS transmission measurements may be approximately 10% lower than the Mie theory value [19]. The normalized intensity autocorrelation functions are shown in Figure 2.13. A comparison of the intensity and electric field autocorrelation functions is shown in Figure 2.14. At long time delay times, the intensity autocorrelation function is smoother, so this function was used for data fitting along with an l^* of 235 μm . It was assumed that $z_0 = l^*$. Nonlinear least squares with one parameter was performed in Matlab® using the ‘lsqcurvefit’ function and the 90% confidence interval was found using the ‘nlparci’ function. The former function generates parameters using the levenberg-marquardt algorithm [20, 21, 22] and the latter function uses the parameter estimates, residuals, and coefficient covariance matrix to generate the confidence interval.

The fits to the intensity autocorrelation function for point source and plane wave are shown in Figures 2.15 and 2.16, respectively. For plane wave, the viscosity of water at 20 °C was determined to be $1.0 \pm 2.5 \times 10^{-2}$ mPa.s. For point source, the viscosity of water at 20 °C was determined to be $0.95 \pm 3.1 \times 10^{-2}$ mPa.s. The fit values are within 6% of the expected viscosity of water at 20 °C[23].

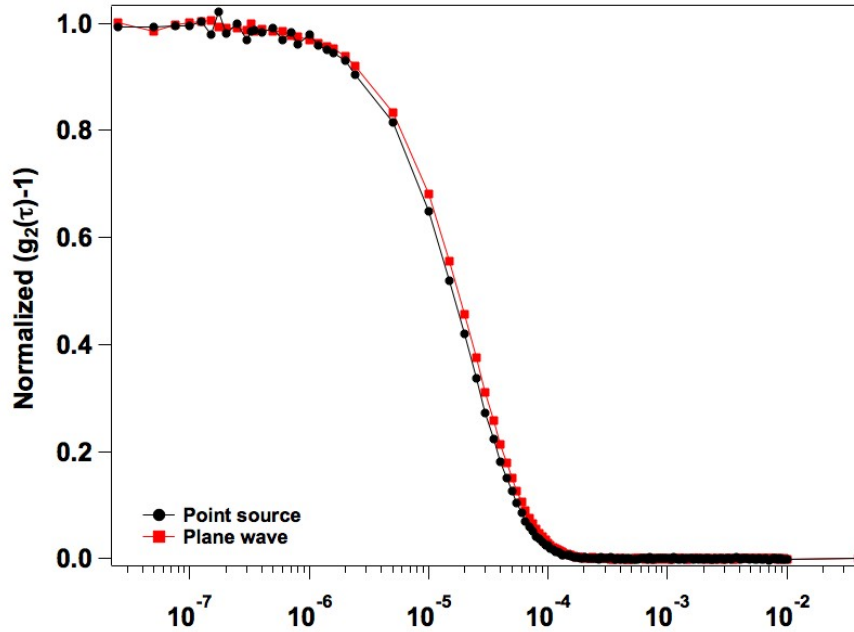


Figure 2.13: Experimental $g_2(\tau) - 1$ for 1.05 vol% polystyrene spheres in a 4.5 mm cuvette in plane wave and point source transmission mode.

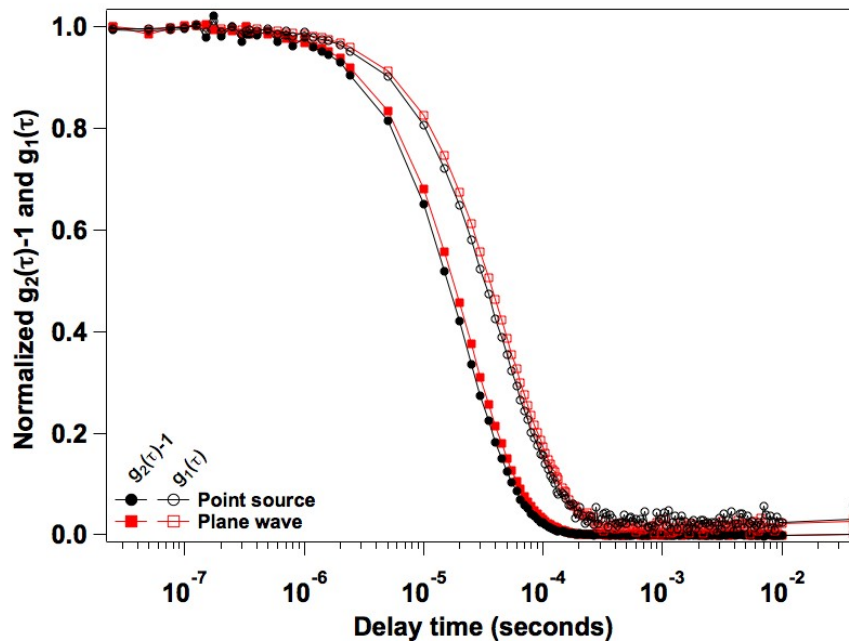


Figure 2.14: Experimental $g_2(\tau) - 1$ and $g_1(\tau)$ for 1.05 vol% polystyrene spheres in a 4.5 mm cuvette in plane wave and point source transmission mode.

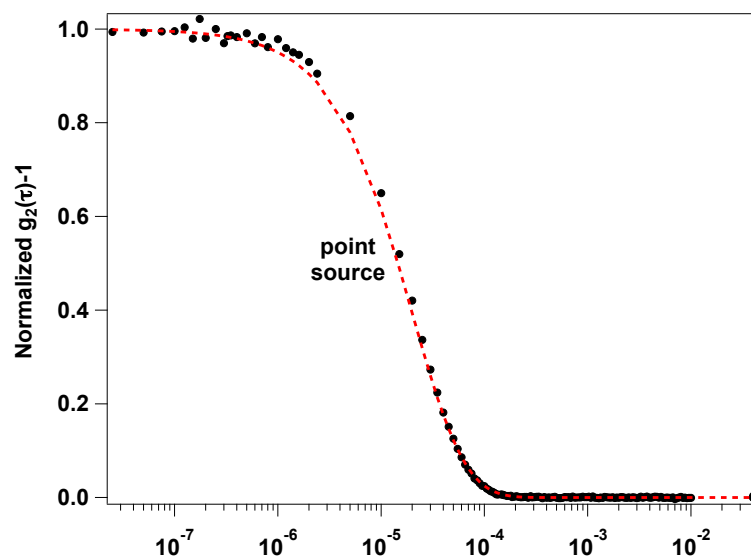


Figure 2.15: Experimental $g_2(\tau) - 1$ for 1.05 vol% polystyrene spheres in a 4.5 mm cuvette in point source transmission with fit.

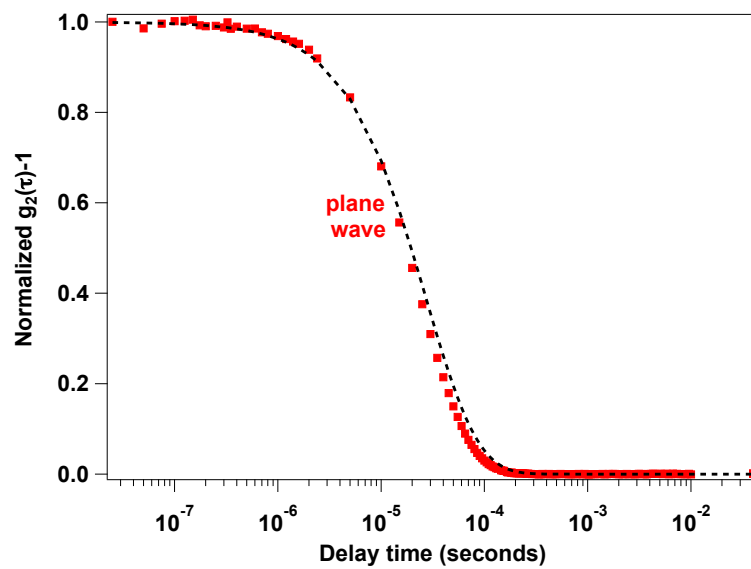


Figure 2.16: Experimental $g_2(\tau) - 1$ for 1.05 vol% polystyrene spheres in a 4.5 mm cuvette in plane wave transmission with fit.

2.9 Data Analysis of a Viscoelastic Fluid

A model viscoelastic fluid was used to validate the high-pressure cell at atmospheric pressure in point source transmission mode. The intensity autocorrelation functions are shown in Figure 2.17. As the wt% of PEO is increased, the onset of the intermediate decay region shifts right. From refractometry measurements, the refractive index increases with PEO wt%, which may increase the l^* value and cause a slight shift to longer delay times. However, the shift right is better explained by an increase in viscosity. In addition to the shift, the shape of the autocorrelation function changes, which corresponds to viscoelastic behavior. The intermediate decay region was fit and the mean square displacement (MSD) was determined from numerical integration and is shown scaled by the probe radius in Figure 2.18. The concentrations of PEO are above the overlap concentration and the viscoelasticity is attributed to entanglement of the polymer coils[12]. The overlap concentration, signaling the transition from the dilute to semidilute regime, for 200 kDa PEO is approximately 0.5 wt% [12]. The logarithmic slope of the MSD is an indication of the viscoelasticity of a sample. A logarithmic slope of 1 corresponds to purely viscous and a logarithmic slope of 0 corresponds to purely elastic. At short delay times, the 6.7 and 12.2 wt% PEO samples have smaller slopes than at longer delay times indicating a shift from a more elastic to a more viscous response.

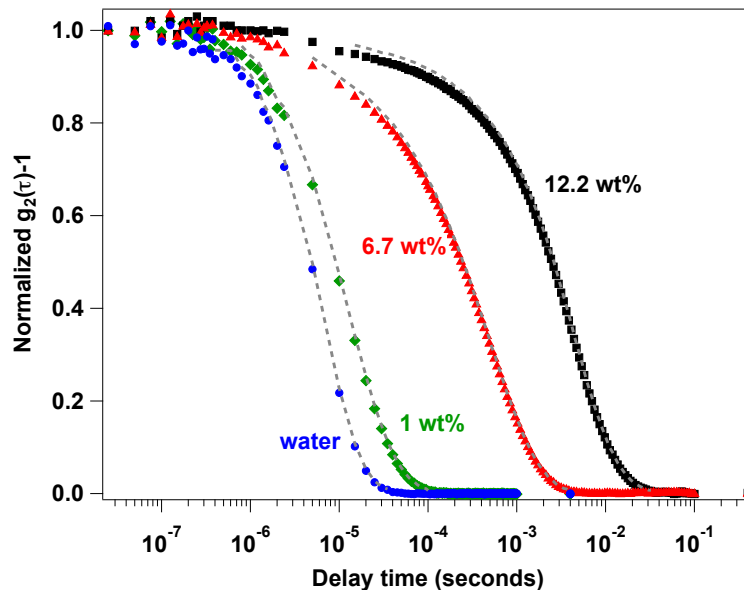


Figure 2.17: Normalized $g_2(\tau) - 1$ for 1, 6.7, and 12.2 wt% 200 kDa PEO with 1 wt% 1 μm polystyrene spheres at 21°C in the HPC. The intermediate decay region was fit as denoted by the dotted line. Water is shown for reference.

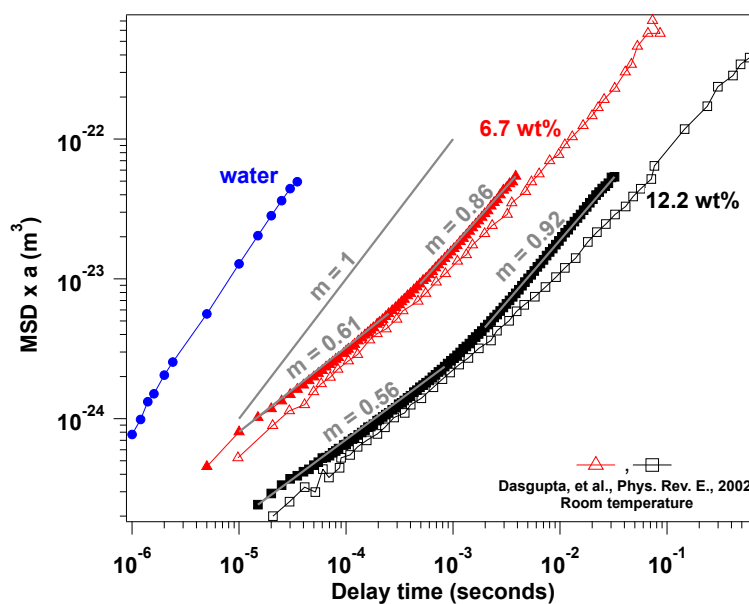


Figure 2.18: The mean square displacement (MSD) scaled by probe radius for 6.7, and 12.2 wt% 200 kDa PEO compared to literature data[12]. Water and logarithmic slope of 1 are shown for reference.

REFERENCES

- [1] Y. Cheng, K. M. Brown, and R. K. Prud'homme. Characterization and intermolecular interactions of hydroxypropyl guar solutions. *Biomacromolecules*, 3(3): 456–461, 2002.
- [2] J. Chatterji and J. K. Borchardt. Applications of water-soluble polymers in the oil field. *Journal of Petroleum Technology*, 33(11):2042, 1981.
- [3] P. L. R. Cunha, R. C. M. dePaula, and J. P. A. Feitosa. Purification of guar gum for biological applications. *International Journal of Biological Macromolecules*, 41(3):324–331, 2007.
- [4] M. K. Dufficy. *Binders and Hosts for High-Capacity Lithium-ion Battery Anodes*. PhD thesis, North Carolina State University, 2016.
- [5] S. Kesavan and R. K. Prud'homme. Rheology of guar and HPG cross-linked by borate. *Macromolecules*, 25(7):2026–2032, 1992.
- [6] R. R. Mallepally, V. S. Gadepalli, B. A. Bamgbade, N. Cain, and M. A. McHugh. Phase behavior and densities of propylene + hexane binary mixtures to 585 K and 70 MPa. *Journal of chemical and engineering data*, 61(8):2818–2827, 2016.
- [7] C. J. Kloxin. *Investigating aqueous PEO-PPO-PEO Triblock Copolymer Dispersion Dynamics With Colloidal Sphere Thermal Motion*. PhD thesis, North Carolina State University, 2006.
- [8] C. J. Kloxin and J. H. van Zanten. High pressure phase diagram of an aqueous PEO-PPO-PEO triblock copolymer system via probe diffusion measurements. *Macromolecules*, 43(4):2084–2087, 2010.

- [9] T. W. Kermis, D. Li, O. Guney-Altay, I. Park, J. H. van Zanten, , and M. A. McHugh. High-pressure dynamic light scattering of poly(ethylene-co-1-butene) in ethane, propane, butane, and pentane at 130 °C and kilobar pressures. *Macromolecules*, 37(24):9123–9131, 2004.
- [10] E. R. Dobrovinskaya, L. A. Lytvynov, and V. Pishchik. *Sapphire: Material, Manufacturing, Applications*. Springer, 2009.
- [11] D. J. Pine, D. A. Weitz, P. M. Chaikin, and E. Herbolzheimer. Diffusing wave spectroscopy. *Physical Review Letters*, 60(12):1134–1137, 1988.
- [12] B. R. Dasgupta, S. Tee, J. C. Crocker, B. J. Frisken, and D. A. Weitz. Microrheology of polyethylene oxide using diffusing wave spectroscopy and single scattering. *Physical Review E*, 65(5):051505, 2002.
- [13] B. R. Dasgupta and D. A. Weitz. Microrheology of cross-linked polyacrylamide networks. *Physical Review E*, 71(2):021504, 2005.
- [14] R. G. Alargova, S. Deguchi, and K. Tsujii. Dynamic light scattering study of polystyrene latex suspended in water at high temperatures and high pressures. *Colloids and Surfaces A: Physicochemical and Engineering Aspects*, 183-185:303–312, 2001.
- [15] S. I. Sandler. *Chemical, Biochemical, and Engineering Thermodynamics*. John Wiley & Sons, 4th edition, 2006.
- [16] J. Brandrup and E. H. Immergut, editors. *Polymer Handbook*. John Wiley & Sons, 3rd edition, 1989.
- [17] E. M. Furst and T. M. Squires. *Microrheology*. Oxford University Press, 2017.
- [18] M. H. Lee and E. M. Furst. Formation and evolution of sediment layers in an aggregating colloidal suspension. *Physical Review E*, 74(3):031401, 2006.

- [19] D. J. Pine, D. A. Weitz, J. X. Zhu, and E. Herbolzheimer. Diffusing-wave spectroscopy: dynamic light scattering in the multiple scattering limit. *Journal de Physique*, 51(18):2101–2127, 1990.
- [20] K. Levenberg. A method for the solution of certain non-linear problems in least-squares. *Quarterly of Applied Mathematics*, 2(2):164–168, 1944.
- [21] D. W. Marquardt. An algorithm for least-squares estimation of nonlinear parameters. *Journal of the Society of Industrial and Applied Mathematics*, 11(2):431–441, 1963.
- [22] J. J. More. *Numerical Analysis- The Levenberg-Marquardt Algorithm: Implementation and Theory*. Ed. by G.A. Watson. Springer-Verlag Berlin Heidelberg, 1978.
- [23] J. Kestin, M. Sokolov, and W. A. Wakeham. Viscosity of liquid water in the range -8 °C to 150 °C. *Journal of Physical and Chemical Reference Data*, 7(3):941–948, 1978.

Chapter 3

VISCOSITY OF 1-PROPANOL-WATER MIXTURES

The following section describes the high-pressure viscosity measurement of water and an aqueous 1-propanol mixture to validate the high-pressure cell.

3.1 High-pressure Water Viscosity

Water is a common solvent in many complex fluids that are subjected to environmental and processing conditions at elevated pressure. Previous studies [1, 2, 3] have demonstrated that the viscosity of water is a weak function of pressure. Moreover, most liquids show an increase in viscosity with pressure, but, water exhibits an anomalous viscosity minimum. This minimum has been explained by distortion of the hydrogen bond network followed by increased packing [2] and structure breaking [3] and is a stronger function of temperature than pressure.

High-pressure experiments with ultra pure water were performed to validate the high-pressure cell in point source and transmission mode. Due to the longer pathlength of the high-pressure cell, 0.5 vol % polystyrene beads was used to achieve a detection rate of approximately 100 kilocounts per seconds (kcps). The normalized intensity autocorrelation functions as a function of pressure are shown in Figure 3.1. The inset shows that the functions fall between the pressure extremes. From Mie theory, the l^* is $534 \mu\text{m}$. The fits to the lowest and highest pressure intensity autocorrelation functions were performed using $l^* = 490 \mu\text{m}$ and are shown in Figure 3.2. For 0 MPag, the viscosity of water at $21 \text{ }^\circ\text{C}$ was determined to be $0.95 \pm 1.4 \times 10^{-2} \text{ mPa}\cdot\text{s}$. For 172.4 MPag, the viscosity of water at $21 \text{ }^\circ\text{C}$ was determined to be $0.95 \pm 2.1 \times 10^{-2} \text{ mPa}\cdot\text{s}$. The fit values are within 5% of the expected viscosity of water at $21 \text{ }^\circ\text{C}$ [4]. The high

pressure viscosity is also compared to the NIST Chemistry WebBook[5] and shows good agreement as reported in Figure 3.3.

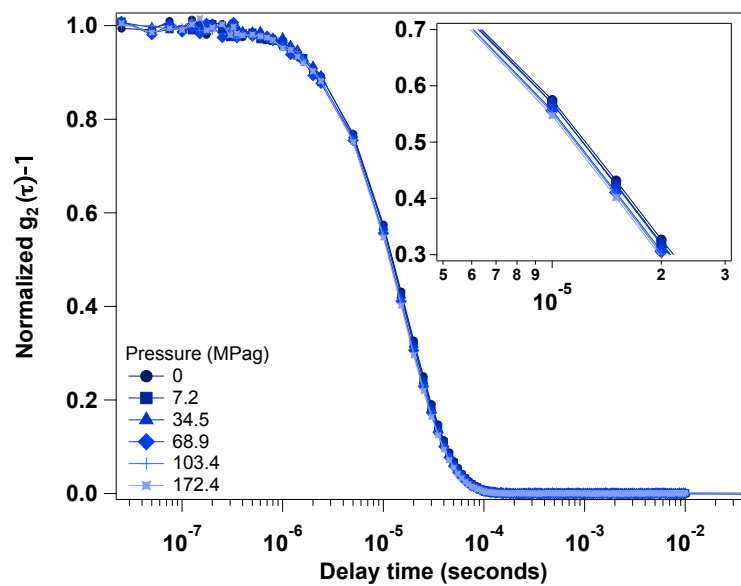


Figure 3.1: Normalized $g_2(\tau) - 1$ for 0.5 vol% polystyrene beads in water in the high-pressure cell.

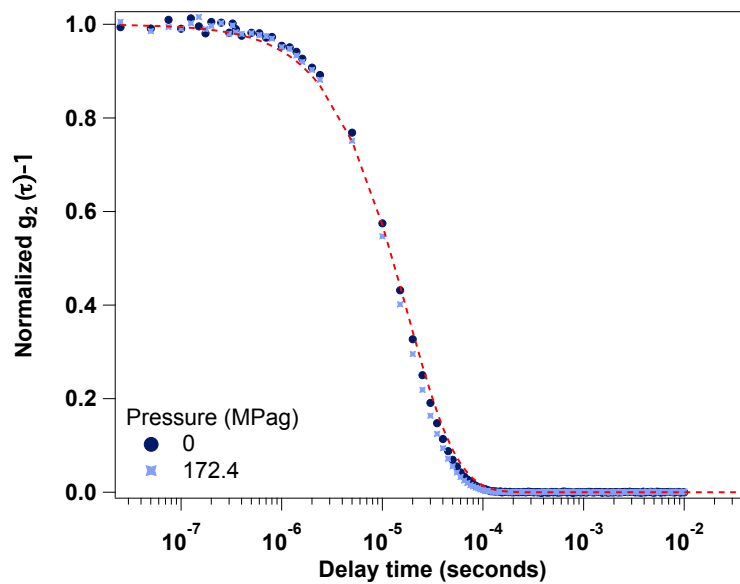


Figure 3.2: Normalized $g_2(\tau) - 1$ for 0.5 vol% polystyrene beads in water in the high-pressure cell with fit.

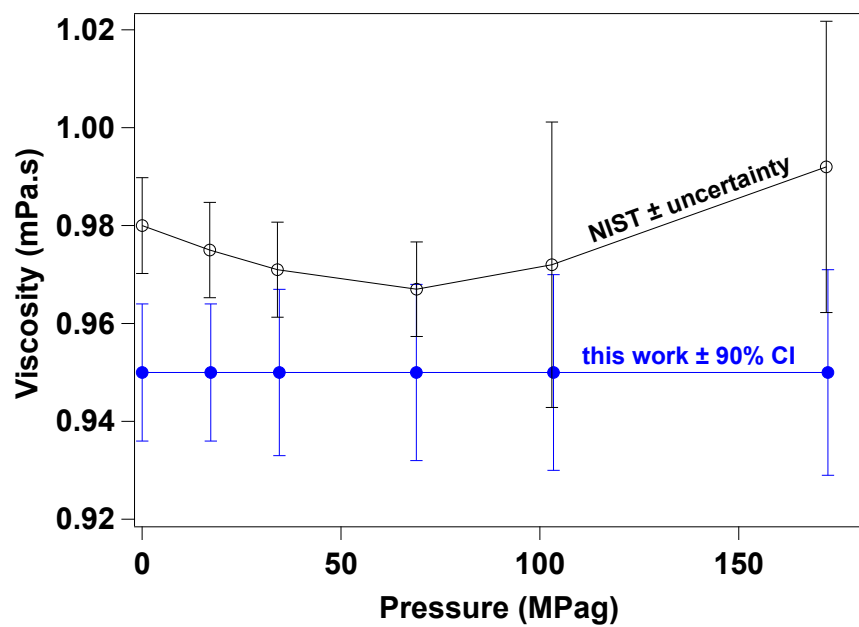


Figure 3.3: High-pressure water viscosity at 21°C.

3.2 High-pressure Aqueous 1-Propanol Viscosity

The viscosity of pure alcohols and aqueous solutions of alcohols has been shown to increase with pressure as shown with measurements using a falling-cylinder viscometer [6]. 1-propanol, shown in Figure 3.4, was selected for a validation experiment using a Newtonian fluid. The values in literature ($\sim 2\text{-}7$ mPa.s) are within the DWS operating regime and the system is purely viscous, which eliminates potential non-continuum effects. A key concern is the stability of the polystyrene probes in 1-propanol. To verify stability, multiple particle tracking experiments were performed with an example image shown in Figure 3.5. The probes show no measurable degree of aggregation suggesting good stability.

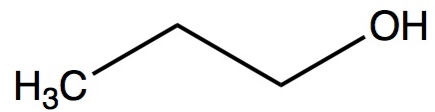


Figure 3.4: Chemical structure of 1-propanol.

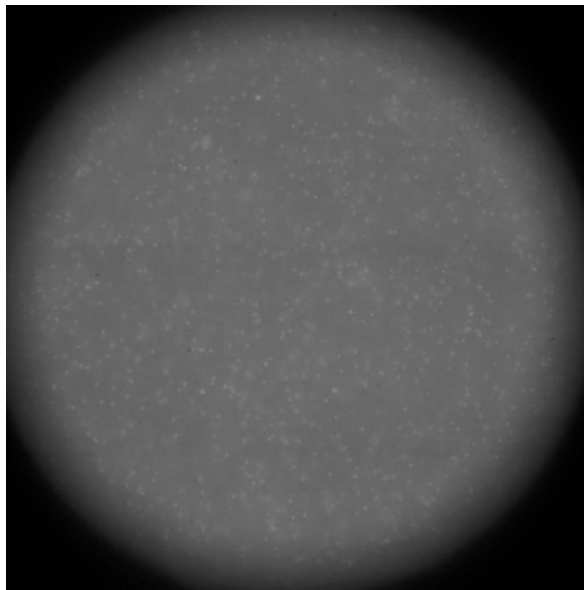


Figure 3.5: An image of fluorescent micrometer-diameter polystyrene spheres in 1-propanol that shows the probes are colloidally stable.

Intensity autocorrelation functions as a function of pressure for polystyrene probes in aqueous 1-propanol are shown in Figure 3.6. As pressure increases, the onset of the intermediate decay region shifts to the right, which is consistent with an increase in viscosity. For a preliminary analysis, the refractive index is assumed to be constant over the conditions tested. After measurements at the maximum pressure of 103.4 MPag, the pressure was reduced slowly to repeat measurements at 68.9 and 0 MPag to investigate hysteresis. The inset of Figure 3.6 shows that the normalized intensity autocorrelation function shifts slightly to longer delay times after pressure is removed to 0 MPag. The refractive index of the aqueous 1-propanol mixture was estimated to be 1.37 using a weighted average of pure fluids and from Mie theory, the l^* is $784 \mu\text{m}$. The fits to the intensity autocorrelation functions are shown in Figure 3.7 using $l^* = 700 \mu\text{m}$. The fit viscosities as a function of pressure are shown in Figure 3.8 with confidence intervals. Literature data for 0.75 and 1 mole fraction 1-propanol at 10 and 25 °C[6] was used to linearly interpolate for viscosity values for 0.84 mole fraction 1-propanol at 21 °C as a function of pressure. Overall, there is good agreement between experimental and literature values for 0.84 mole fraction 1-propanol at 21 °C .

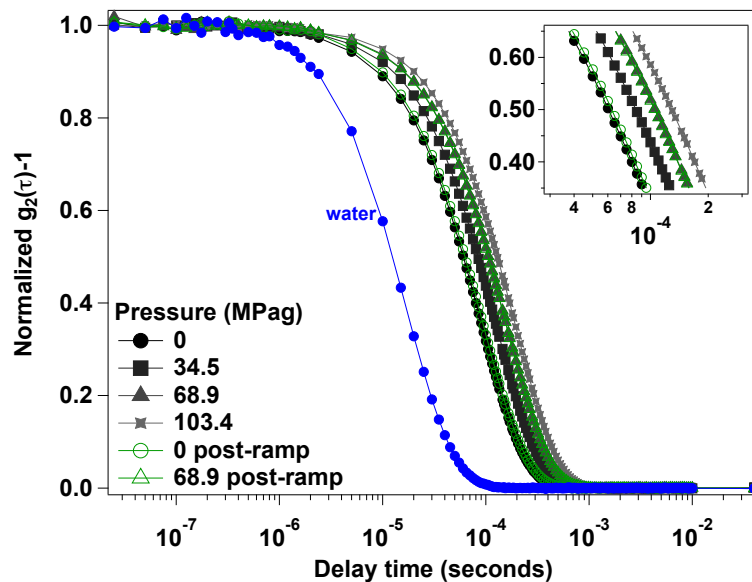


Figure 3.6: Experimental $g_2(\tau) - 1$ for 0.5 vol% polystyrene beads in 1-propanol with a mole fraction of 0.84 as a function of pressure. Open circle and triangles show repeat experiment after pressure ramp. Water is shown for reference.

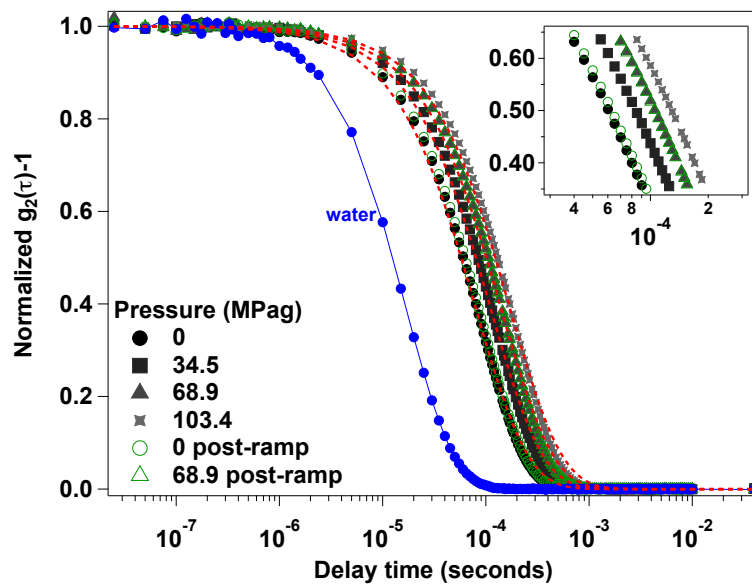


Figure 3.7: Experimental $g_2(\tau) - 1$ for 0.5 vol% polystyrene beads in 1-propanol with a mole fraction of 0.84 as a function of pressure with fit. Water shown for reference.

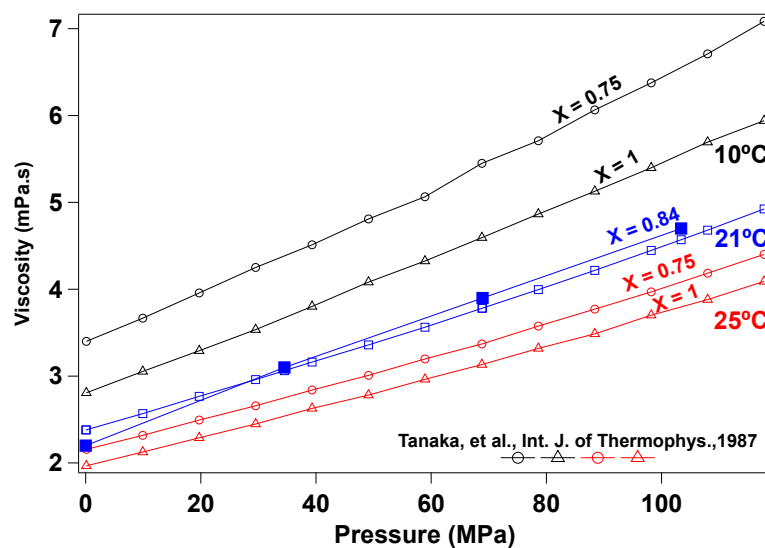


Figure 3.8: Experimental data (filled) with 90% confidence intervals (smaller than points) at 21°C and literature data at 10 and 25 °C [6] showing pressure dependence of aqueous 1-propanol solutions. Data for 21 °C were linearly interpolated.

REFERENCES

- [1] P. Forst, F. Werner, and A. Delgado. The viscosity of water at high pressures - especially at subzero degrees centigrade. *Rheologica Acta*, 39(6):566–573, 2000.
- [2] T. DeFries and J. Jonas. Pressure dependence of NMR proton spin–lattice relaxation times and shear viscosity in liquid water in the temperature range -15–10 °C. *The Journal of Chemical Physics*, 66(3):896–901, 1977.
- [3] R. A. Horne and D. S. Johnson. The viscosity of water under pressure. *The Journal of Physical Chemistry*, 70(7):2182–2190, 1966.
- [4] J. Kestin, M. Sokolov, and W. A. Wakeham. Viscosity of liquid water in the range -8 °C to 150 °C. *Journal of Physical and Chemical Reference Data*, 7(3):941–948, 1978.
- [5] E. W. Lemmon, M. O. McLinden, and D. G. Friend. *NIST Chemistry WebBook, NIST Standard Reference Database: Thermophysical Properties of Fluid Systems*. Number 69. National Institute of Standards and Technology, Gaithersburg MD, 20899, (retrieved September 22, 2017).
- [6] Y. Tanaka, Y. Matsuda, H. Fujiwara, H. Kubota, and T. Makita. Viscosity of (water + alcohol) mixtures under high pressure. *International Journal of Thermophysics*, 8(2):147–163, 1987.

Chapter 4

CONCLUSIONS AND FUTURE WORK

4.1 Conclusions

Environmental and processing conditions expose complex fluids to a range of pressures that may affect performance and rheological properties. High-pressure rheology is typically performed using mechanical rheometry with pressure driven, falling-body, and rotational devices. However, these techniques may be limited to pressures that are lower than applications of interest and restricted to Newtonian fluids. To address these limitations, a high-pressure light scattering microrheology experiment is designed and validated with the pressure dependent viscosity of 1-propanol at pressures up to 103.4 MPa. The high-pressure application of interest to this work is hydraulic fracturing using linear and borate crosslinked guar gum. Preliminary work is discussed below for obtaining the high-pressure behavior of guar gum. Future work includes modifying the experimental procedure to determine λ^* , assessing different loading procedures to increase operating regime, and accounting for nonergodicity of highly crosslinked samples. In addition, other materials of interest such as borate crosslinked poly(vinyl) alcohol may be assessed for pressure dependent viscoelasticity.

4.2 Physically Crosslinked Guar Gum Under Pressure

The fracturing fluid components of interest are linear and borate crosslinked guar gum due to their wide use [1] and the observed pressure dependence [2]. The guar gum chemical structure and borate crosslinking mechanism are shown in Figures 4.1 and 4.2. Crosslinking between guar gum and boron is chemical in nature, but may be considered physical crosslinking due to the equilibrium of bonds breaking and reforming, which gives the system self-healing properties [3]. This crosslinking reaction

is heavily dependent on pH, temperature, and concentration of borate and polymer [3]. Depending on the pH, the crosslinked guar gum may exhibit fluid-like (pH \sim 7) or solid-like (pH \sim 9) behavior, however only significant crosslinking occurs above pH 8 [4].

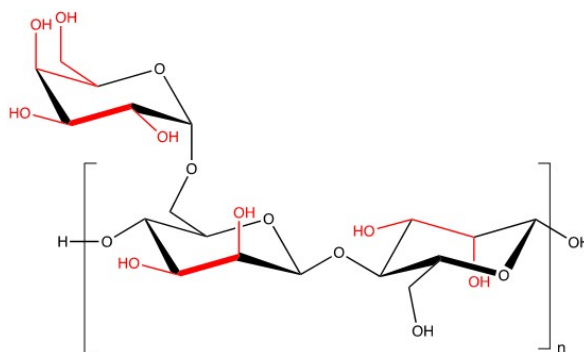


Figure 4.1: Guar gum with vicinal hydrogens highlighted in red.

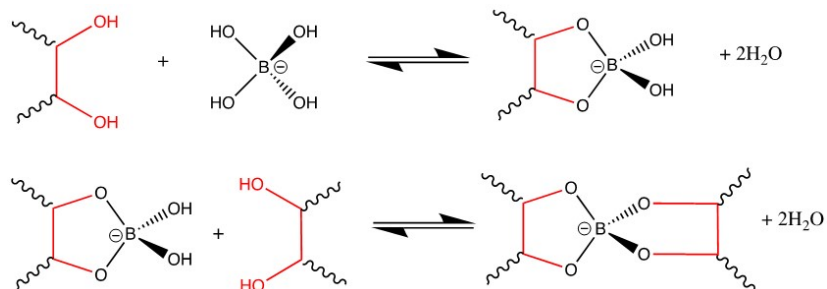


Figure 4.2: Adapted figure of physical crosslinking of vicinal hydroxyls by borate from a 1:1 complex (top) to a 2:1 complex (bottom) [3].

Current high-pressure loading methods have been optimized to prevent the introduction of air to samples and to remove air from the system. However, the loading procedure limits the modulus of samples that may be tested. During preliminary experiments, it was found that samples of 0.3 wt % guar gum with 60 ppm boron could not be loaded into the cell. The proposed modified operating regime for this device is shown in Figure 4.3 based on duplicate mechanical rheometry oscillatory strain measurements. The modulus values were obtained from the linear viscoelastic region with an example shown in Figure 4.4. The upper limit was determined to be 3 ± 0.1 Pa for trial 1 and 3.1 ± 0.1 Pa for trial 2. Difficulties loading the heavily crosslinked sample into the rheometer are noted and the observed viscoelastic behavior is shown in Figures 4.5 and 4.6. In addition, a visual operating regime was generated as shown in 4.7. Strong viscoelastic behavior was noted by moving a magnetic stir bar embedded in the sample.

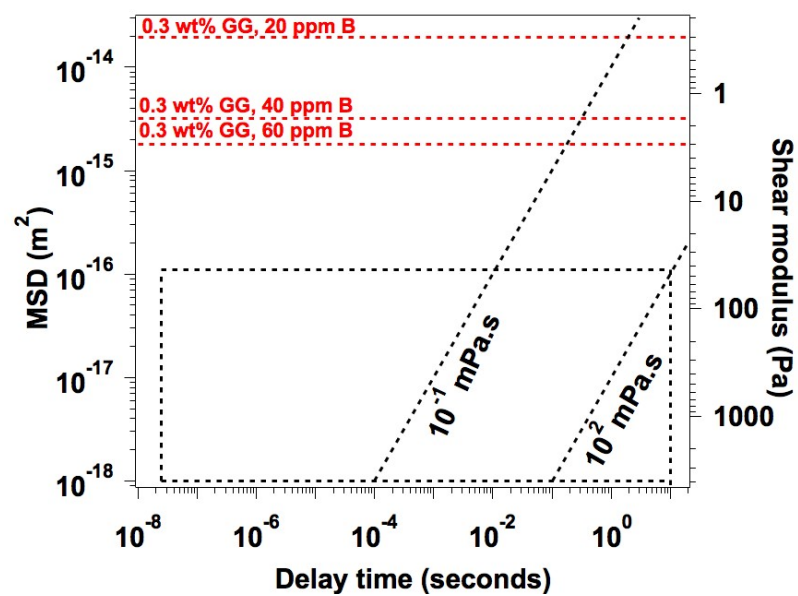


Figure 4.3: Modified loading limit for high-pressure diffusing wave spectroscopy instrument.

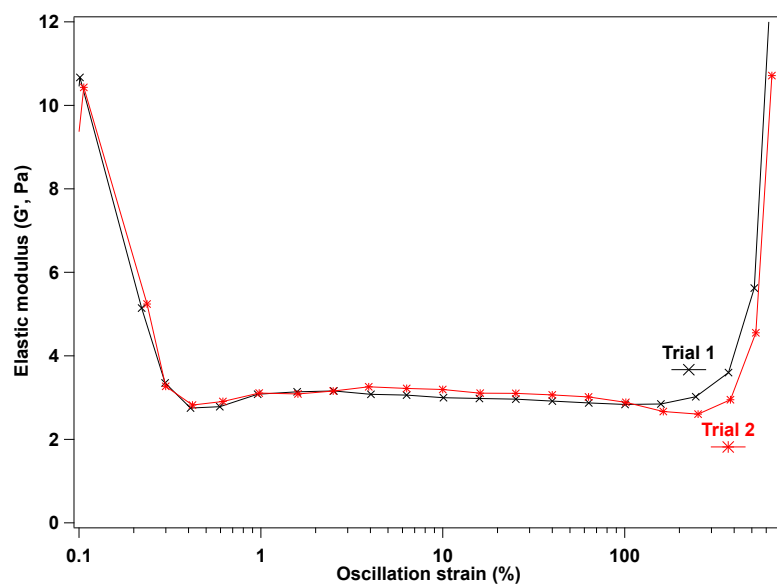


Figure 4.4: Elastic modulus for 0.3 wt% purified guar gum with 60 ppm boron determined from mechanical rheometry using a 60 mm, 2° cone.



Figure 4.5: Image of 0.3 wt% guar gum with 60 ppm boron. Geometry shown is a 40 mm 4° cone and peltier plate.



Figure 4.6: Image of 0.3 wt% guar gum with 40 ppm boron. Geometry shown is a 40 mm 4° cone and peltier plate.

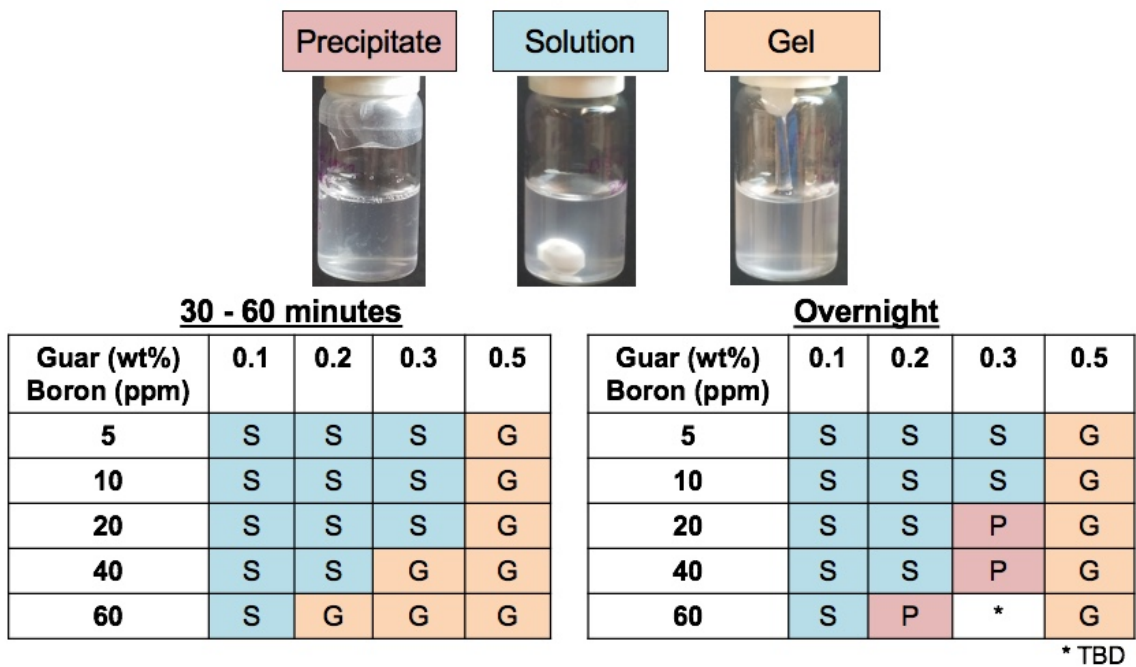


Figure 4.7: Visual operating regime for precipitate (P), solution (S), and gel (G). Observations taken at 30-60 minutes and again overnight.

Preliminary high-pressure data has been collected for purified guar gum and borate crosslinked guar gum and is shown in Figures 4.8 and 4.9. Figure 4.8 shows that increasing the polymer wt% corresponds to an increase in the decay onset consistent with an increase in viscosity. In addition, the shape of the intensity autocorrelation functions changes with respect to water at the end of the intermediate decay region consistent with viscoelastic behavior. There is an anticipated weak pressure dependence possibly due to hydrogen bonding. Figure 4.9 shows that there is an increase in the decay onset with 20 ppm boron, consistent with increasing viscoelasticity. However, the normalized intensity autocorrelation functions do not demonstrate a strong pressure dependence, which is unexpected based on literature [2]. The microscopic creep compliance for intermediate delay times is shown in Figure 4.10. The crosslinker concentration was lower than the 60 ppm reported in literature [2] due to sample loading constraints, but sufficient viscoelasticity was observed. It is possible that the purification method may have a stronger impact on the guar gum than previously noted. In addition, the strong pressure dependence may only occur with higher crosslink density.

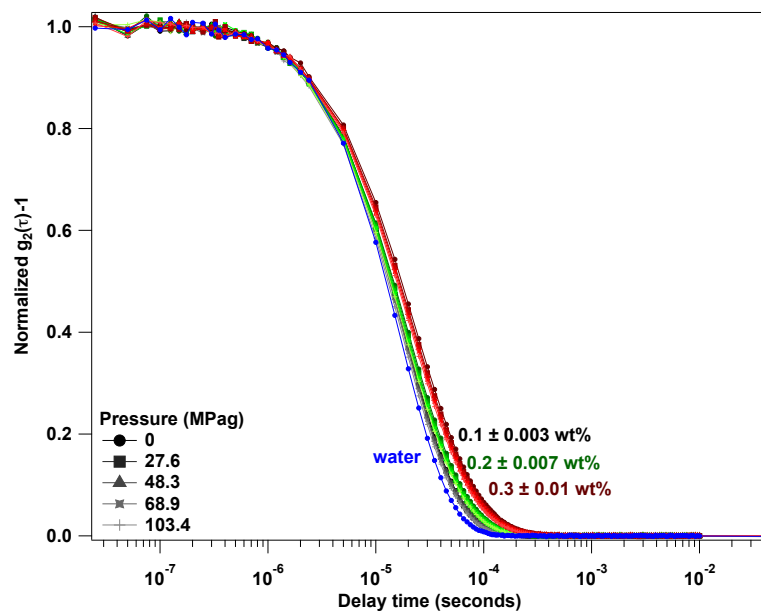


Figure 4.8: Normalized $g_2(\tau) - 1$ for purified guar gum with 0.5 vol% polystyrene spheres. Water is shown for reference.

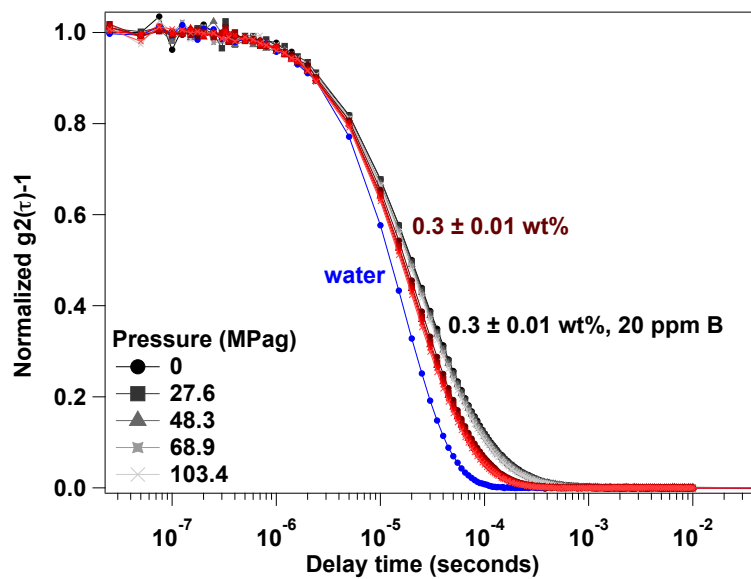


Figure 4.9: Normalized $g_2(\tau) - 1$ for crosslinked guar gum with 20 ppm boron and 0.5 vol% polystyrene spheres. Water is shown for reference.

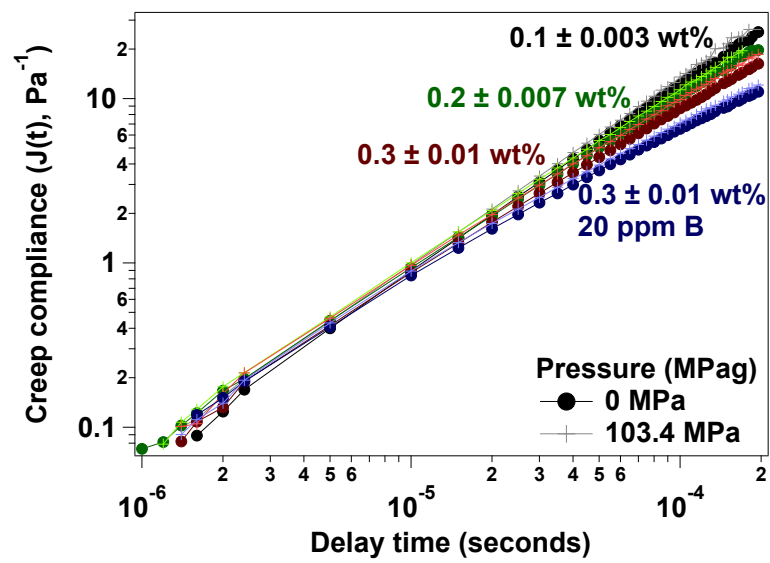


Figure 4.10: Creep compliance for intermediate delay times.

4.3 Experiment Modification

The experimental operating regime may be expanded by adjusting sample loading and experimentally determining l^* . Sample loading may be modified to increase the operating regime. The pH and temperature dependent equilibrium of the borate crosslinks[4, 5] may allow less viscoelastic samples to be loaded before shifting the equilibrium to favor more crosslinks. For example, a heavily crosslinked sample may be loaded after decreasing the crosslink density by increasing temperature [5]. As the system equilibrates to room temperature, the reaction equilibrium would be expected to shift and favor crosslinks, thus increasing the viscoelastic properties. An alternative approach would be to include a membrane within the cell that would allow borate ions to diffuse into a guar gum solution. To reduce the number of parameters in the nonlinear least square fit, the value of l^* may be obtained experimentally [6, 7, 8, 9]. The l^* of an unknown sample is obtained using a reference sample and

$$l^* = \frac{T l_{\text{ref}}^*}{T_{\text{ref}} + \frac{4I_{\text{ref}}^*}{3L} (T_{\text{ref}} - T)} \quad (4.1)$$

with reference transmission T_{ref} and l^* and unknown sample transmission T and mean free path l^* with identical sample thickness L .

The experimental setup may be modified to account for nonergodicity and temperature dependence. DWS requires that the system be ergodic or that the ensemble average is equal to the time average. However, if a system is more solid-like as observed with heavily crosslinked gels, then the probe particle motion may be restricted resulting in nonergodicity. DWS may be extended to nonergodic media using the two cell technique [10]. The technique employs two turbid media with one being ergodic and placed after the nonergodic sample. Scheffold et al. demonstrate that the light transmitted may still be considered ergodic even if only the second cell is ergodic[10]. The experimental setup will be modified as described by Panczyk[11]. A gridded or opal disk is placed in the beam path before the nonergodic sample. The disk is rotated with a stepper motor (VEXTA Model PK564AW) powered by a driver

(Model RKD514L-C) and controlled by a controller (VEXTA Model EMP 401) from Oriental Motor Co. Ltd. The resulting autocorrelation function will include the motion of the disk. The disk and particle motion are decoupled using

$$g_1^{\text{sample}} = \frac{g_1^{\text{sample+disk}}}{g_1^{\text{disk}}}. \quad (4.2)$$

After assessing high-pressure experiments, work will progress to high-pressure and high-temperature experiments. Temperature capabilities will be added to the cell using a flexible heater. A thermocouple modified for high-pressure will be inserted into the top high-pressure cell port to monitor temperature.

4.4 Borate Crosslinked Poly(vinyl) Alcohol

Borate may also be used to crosslink poly(vinyl) alcohol (PVA), with structure shown in Figure 4.11. A pressure dependent viscosity has also been reported [2].

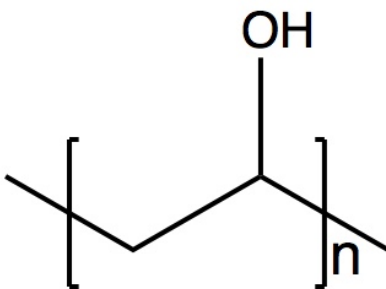


Figure 4.11: Poly(vinyl) alcohol structure.

REFERENCES

- [1] R. Barati and J. Liang. A review of fracturing fluid systems used for hydraulic fracturing of oil and gas wells. *Journal of Applied Polymer Science*, 131(16):40735, 2014.
- [2] M. D. Parris, B. A. MacKay, J. W. Rathke, R. J. Klingler, and R. E. Gerald II. Influence of pressure on boron cross-linked polymer gels. *Macromolecules*, 41(21): 8181–8186, 2008.
- [3] E. Pezron, A. Ricard, and L. Leibler. Rheology of galactomannan-borax gels. *Journal of Polymer Science: Part B: Polymer Physics*, 28:2445–2461, 1990.
- [4] S. Kesavan and R. K. Prud’homme. Rheology of guar and HPG cross-linked by borate. *Macromolecules*, 25(7):2026–2032, 1992.
- [5] E. Pezron, L. Leibler, A. Ricard, and R. Audebert. Reversible gel formation induced by ion complexation. 2. phase diagrams. *Macromolecules*, 21(4):1126–1131, 1988.
- [6] B. R. Dasgupta, S. Tee, J. C. Crocker, B. J. Frisken, and D. A. Weitz. Microrheology of polyethylene oxide using diffusing wave spectroscopy and single scattering. *Physical Review E*, 65(5):051505, 2002.
- [7] D. A. Weitz and D. J. Pine. *Dynamic Light Scattering: Diffusing-wave spectroscopy*. Ed. W. Brown. Oxford University Press Inc., 1993.
- [8] E. M. Furst and T. M. Squires. *Microrheology*. Oxford University Press, 2017.

- [9] P. D. Kaplan, A. D. Dinsmore, A. G. Yodh, and D. J. Pine. Diffuse-transmission spectroscopy: A structural probe of opaque colloidal mixtures. *Physical Review E*, 50(6):4827–4835, 1994.
- [10] F. Scheffold, S. E. Skipetrov, S. Romer, and P. Schurtenberger. Diffusing-wave spectroscopy of nonergodic media. *Physical Review E*, 63:061404, 2001.
- [11] M. M. Panczyk. *Directed assembly and dynamics of anisotropic particles*. PhD thesis, University of Delaware, 2013.

Appendix

LASER MAINTENANCE

The Argon ion laser used in this study provides sufficient power to allow for diffusing wave spectroscopy experiments. Throughout this work, modifications were made to the laser setup including valve addition for maintaining proper cooling water temperature and cleaning the Brewster windows.

Laser specifications require the cooling fluid to be between 10-35 °C at a flow rate of 8.5-11.5 liters per minute[1]. Proper cooling is essential to maintaining the laser and preventing overheating. During the initial system start-up, cooling water is pumped through the system before the laser is turned on to ensure proper water flow and temperature. After the laser is turned on the cooling water temperature rises due to heat transfer from the laser. The original pump configuration had water <10°C flowing through the system before the laser was turned on. Water at too low of a temperature may cause condensation resulting in system failure. To correct the inlet water temperature, a valve was added to the water pump as shown in Figure A.1. This valve restricts or allows access to room temperature water or cooled water from a heat exchanger. During start-up, the valve is closed to the heat exchanger and opened once the laser is turned on.

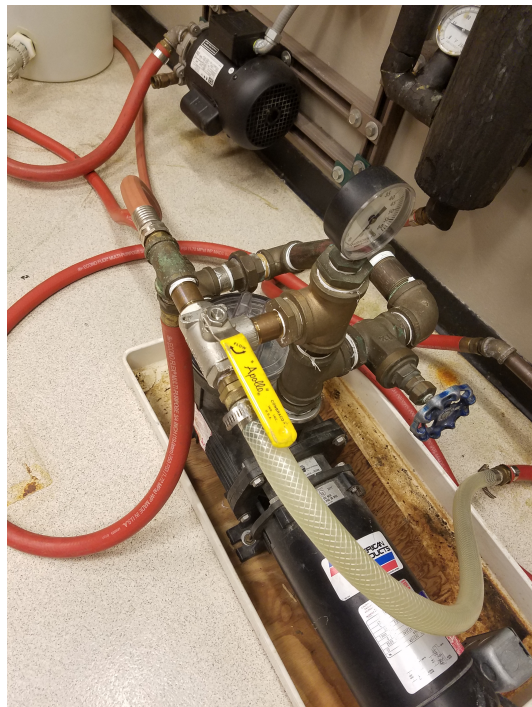


Figure A.1: Image of new pump valve used to restrict or allow access to the cooling water from a heat exchanger.

An indication that the laser is performing abnormally is a decrease in y-intercept of the intensity autocorrelation functions from values of 1. While this effect is normalized out with the dynamical contrast factor (β), it is important to address underlying laser issues. Coherent suggested that a decrease in laser power and deviation from the Gaussian or TEM₀₀ mode was attributed to dirty Brewster windows, high-reflector, beam splitter or output window. The initial laser output is shown in Figure A.2. The laser cavity, depicted in Figure A.3, was opened to reveal the front and rear Brewster windows as shown in Figures A.4 and A.5. The windows were cleaned carefully using the “Hemostat and Lens Tissue Method” [1] with a plastic hemostat and methanol. Brewster window images of before and after cleaning are shown in Figures A.6 and A.7. After cleaning, an increase in power at the same current was observed, however the transverse laser modes were still present.

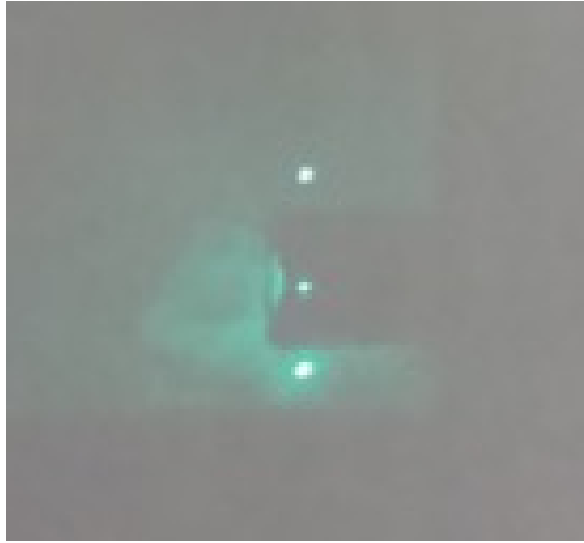


Figure A.2: Image of laser output suggestive of transverse modes.

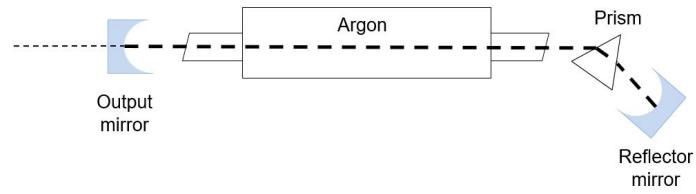


Figure A.3: Schematic of laser cavity. The dotted line indicates the path of the laser beam resonance. All of the laser light is not reflected by the output mirror to allow for lasing.



Figure A.4: Image of front Brewster window facing upwards. This window is cleaned from top to bottom.



Figure A.5: Image of rear Brewster window facing downwards. This window is cleaned from bottom to top.



Figure A.6: Front Brewster window face before cleaning by the “Hemostat and Lens Tissue Method”.



Figure A.7: Front Brewster window face after cleaning by the “Hemostat and Lens Tissue Method”.

To further assess the origin of the transverse laser modes, the aperture wheel, power meter, output mirror, and tuning plate were removed and cleaned as necessary. After reassembly, the laser no longer emitted a beam and instead showed a purple plasma glow because the beam was no longer resonating properly in the tube. To correct the alignment, the “walk-in procedure” was performed [1]. Briefly, this procedure corrects the position of the output and high reflector mirror to align the laser by slowly adjusting the mirrors to maximize power output or mode. It can be challenging to locate the optimal position after the front or rear optics have been removed. The laser beam began resonating again after quickly rocking the high reflector mirror plate while simultaneously tuning the high reflector vertical control. However, the laser pattern shown in A.2 was still apparent. Since the pattern did not change with cleaning and was visible at the laser’s high power output, the spots were attributed to the wedge design of the output coupler. This design prevents back reflections from the laser. The normalized intensity functions from before and after the laser cavity was opened are shown in Figure A.8. There is a slight deviation for 1 mm pathlength before and after and nearly no deviation for a 4.5 mm pathlength sample.

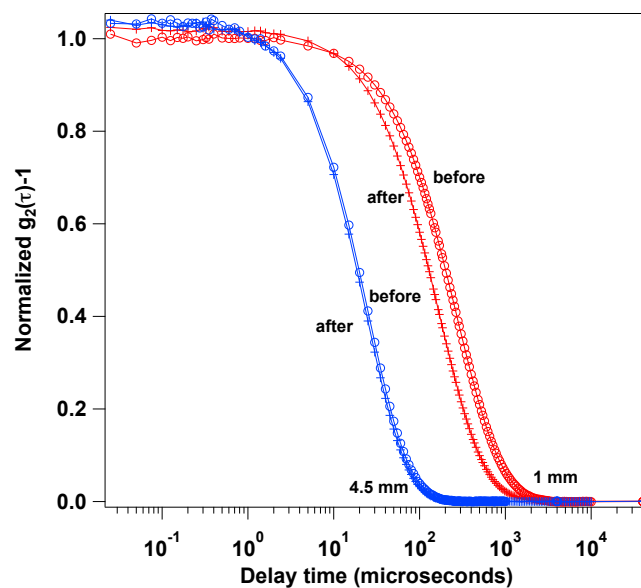


Figure A.8: Normalized $g_2(\tau) - 1$ of samples before and after laser alignment. The sample is 1 vol% $1.04 \mu\text{m}$ polystyrene probes in water in 1 and 4.5 mm cuvettes.

REFERENCES

- [1] Coherent. Operator's manual Innova® 90C series ion laser. Print.